

Luminosity distribution of Type II supernova progenitors

Ósmar Rodríguez^{1*}

¹*School of Physics and Astronomy, Tel Aviv University, Tel Aviv 69978, Israel*

Accepted XXX. Received YYY; in original form ZZZ

ABSTRACT

I present progenitor luminosities (L) for a sample of 112 Type II supernovae (SNe II), computed directly from progenitor photometry and the bolometric correction technique, or indirectly from empirical correlations between progenitor luminosity and [O I] $\lambda\lambda 6300, 6364$ line luminosity at 350 d since explosion, ^{56}Ni mass, or absolute V -band magnitude at 50 d since explosion. To calibrate these correlations, I use twelve SNe II with progenitor luminosities measured from progenitor photometry. I find that the correlations mentioned above are strong and statistically significant, and allow to estimate progenitor luminosities to a precision between 20 and 24 per cent. I correct the SN sample for selection bias and define a subsample of 112 SNe II with progenitor luminosities between $\log(L/L_{\odot}) = 4.6$ dex, corresponding to the completeness limit of the corrected sample, and the maximum observed progenitor luminosity of $\log(L/L_{\odot}) = 5.091$ dex. The luminosity distribution for this subsample is statistically consistent with those for red supergiants (RSGs) in LMC, SMC, M31, and M33 with $4.6 \leq \log(L/L_{\odot}) \leq 5.091$. This supports that SN II progenitors correspond to RSGs. The conspicuous absence of SN II progenitors with $\log(L/L_{\odot}) > 5.1$ dex with respect to what is observed in RSG luminosity distributions, known as the RSG problem, is significant at a $5.2 \pm 0.5 \sigma$ level.

Key words: stars: massive – supergiants – supernovae: general

1 INTRODUCTION

Type II supernovae (SNe II; Minkowski 1941) are the explosions of massive stars with an important amount of hydrogen in their envelope at the moment of explosion. Thus, the classification of an SN as a Type II is based on the presence of H lines in its spectrum. Among SNe II there are some objects showing narrow H emission lines in the spectra, indicative of interaction of the ejecta with circumstellar material (SNe IIn; Schlegel 1990),¹ SNe having long-rising light curves similar to SN 1987A (e.g. Hamuy et al. 1988; Taddia et al. 2016), and some SNe showing peculiar characteristics that make them unique (e.g. OGLE14-073, Terreran et al. 2017; iPTF14hls, Arcavi et al. 2017; ASASSN-15nx, Bose et al. 2018). The rest of events account for about 90 per cent of the SN II population in a volume-limited sample (e.g. Shivers et al. 2017). SNe belonging to the SN IIn and long-rising SN subgroups, and those with peculiar characteristics are not included in the present analysis.

Progenitors of SNe II have been directly identified on pre-explosion images (e.g. Smartt 2009, 2015; Van Dyk 2017), some of them being confirmed as such by their disappearance in late-time high-resolution images. The spectral energy distributions (SEDs) and colour indices of SN II progenitors fit well with those of red supergiant (RSG) stars (e.g. Van Dyk et al. 2003, 2019; Smartt et al. 2004; Maund et al.

2013; O’Neill et al. 2019, 2021). The identification of RSGs as SN II progenitors is consistent with results from pioneering works (e.g. Grassberg et al. 1971; Chevalier 1976; Falk & Arnett 1977), who found that SN II progenitors are stars with large radii and massive H-rich envelopes.

Another important parameter characterizing SN progenitors is the luminosity (L), which is computed from pre-explosion photometry using the bolometric correction (BC) technique or the SED integration. Since progenitors are observed in the final stage of their evolution (a few years before the SN explosion), the observed progenitor luminosity (L_{prog}) is also called final luminosity. The progenitor luminosity, along with an initial mass-final luminosity relation from stellar evolution models, is used to determine the progenitor initial mass M_i (e.g. Smartt et al. 2009; Smartt 2015; and references therein). With the increase in the number of detected progenitors, it became possible to infer properties of the population of RSGs that explode as SNe II. Using a sample of 20 SN II progenitors and assuming a Salpeter initial mass function (IMF), Smartt et al. (2009) derived a maximum initial mass of $16.5 \pm 1.5 M_{\odot}$, which is systematically lower than the maximum RSG mass of around $25 M_{\odot}$. In particular, the authors found that the lack of SN II progenitors with M_i between 17 and $25 M_{\odot}$ with respect to what is expected for a Salpeter IMF is statistically significant at 2.4σ confidence. They termed this discrepancy the “RSG problem”. Later studies, which included new and updated progenitor luminosities (e.g. Smartt 2015; Davies & Beasor 2018,

* E-mail: olrodrig@gmail.com

¹ This group includes SNe IIn/II and LLEV SNe II, described in Rodríguez et al. (2020).

2020), increased the maximum initial mass to 18–19 M_{\odot} ² and set the statistical significance of the RSG problem to around 2σ . Based on the analysis of 24 SN II progenitors, [Davies & Beasor \(2020\)](#) concluded that it is necessary to at least double the sample size to determine whether the RSG problem is statistically significant.

Alternative methods to measure M_i appear as promising tools to increase the number of SNe II with M_i estimates. One of these methods is the age-dating technique (e.g. [Maíz-Apellániz et al. 2004](#); [Murphy et al. 2011](#)), where the age of the stellar population in the SN vicinity is adopted as the age of the progenitor, which allows to estimate its initial mass. This technique has been applied to small SN samples (e.g. [Williams et al. 2014, 2018](#); [Maund 2017](#); [Díaz-Rodríguez et al. 2021](#)). Another method to estimate M_i is by fitting hydrodynamical models to SN light curves (e.g. [Blinnikov et al. 1998](#); [Utrobin 2004](#); [Bersten et al. 2011](#); [Pumo & Zampieri 2011](#); [Morozova et al. 2015](#)). This method has been used to study individual SNe and small SN samples (e.g. [Morozova et al. 2018](#); [Förster et al. 2018](#); [Eldridge et al. 2019](#); [Ricks & Dwarkadas 2019](#); [Martinez & Bersten 2019](#); [Martinez et al. 2020](#); [Utrobin et al. 2021](#)). Recently, [Martinez et al. \(2022\)](#) presented results from hydrodynamical modelling to 53 SNe II, finding a maximum initial mass of 21.3 M_{\odot} . A third alternative method to infer M_i is by comparing late-time spectra with nebular spectra models (e.g. [Jerkstrand et al. 2012, 2014, 2018](#); [Dessart et al. 2021](#)). In particular, the luminosity of the [O I] $\lambda\lambda 6300, 6364$ doublet line ($L_{[\text{O I}]}$) has been shown as a promising observable to estimate M_i (e.g. [Jerkstrand et al. 2014, 2015](#)), while nebular spectra models of [Dessart et al. \(2021\)](#) show a dependence of $L_{[\text{O I}]}$ at 350 d since explosion ($L_{[\text{O I}]}^{350\text{d}}$) on initial mass. This relation arises because $L_{[\text{O I}]}$ depends on ^{56}Ni mass (M_{Ni}) and oxygen mass (e.g. [Elmhamdi et al. 2003](#); [Elmhamdi 2011](#)), where M_{Ni} correlates with M_i (e.g. [Otsuka et al. 2012](#)) while oxygen mass depends on the helium-core mass, which in turns depends on M_i (e.g. [Woosley & Weaver 1995](#)). The method of estimating initial mass by comparing late-time spectra with spectral models has been applied to a small number of SNe (e.g. [Jerkstrand et al. 2012, 2014, 2015, 2018](#); [Silverman et al. 2017](#); [Dessart et al. 2021](#)).

In general, methods to infer M_i require assuming a stellar evolution model, which depends not only on initial mass but also on composition, convection, rotation, mass-loss, binary interaction, among others (e.g. [Eldridge & Tout 2004](#); [Meynet et al. 2015](#); [Limongi & Chieffi 2018](#); [Straniero et al. 2019](#); [Zapartas et al. 2021](#)). Initial mass values computed with the methods mentioned earlier are, therefore, affected by systematic errors related to the stellar evolution modelling and ignorance of the progenitor properties. [Davies & Beasor \(2020\)](#) showed that the SN II progenitor population can be studied in terms of progenitor luminosity instead of initial mass, thus preventing adding the systematic uncertainties mentioned above. In that work, the authors compared the luminosity distribution for SN II progenitors to that observed for RSGs in LMC. This kind of comparison allows to identify similarities and differences between both populations in a

completely empirical way. For example, the RSG problem can be reformulated as the lack of SN II progenitors with luminosity greater than $\log(L/L_{\odot}) = 5.1$ dex (e.g. [Smartt 2015](#)) with respect to what is *observed* in RSG luminosity distributions. On the other hand, the disadvantage of using L_{prog} is that analysis of the luminosity distribution for SN II progenitors is restricted to the small sample of SNe with available progenitor photometry.

An alternative method to increase the number of SNe II with L_{prog} measurements is by inferring L_{prog} indirectly from empirical correlations. [Fraser et al. \(2011\)](#) found a relation between L_{prog} and M_{Ni} , which was also reported by [Kushnir \(2015\)](#). Unfortunately, the authors did not report the strength, significance, or the analytical expression for the observed correlation. Recently, [Davies & Beasor \(2018, 2020\)](#) have presented an updated list of SN II progenitors and their luminosities, while updated M_{Ni} estimates for many of those SNe were reported by [Rodríguez et al. \(2021\)](#). Therefore, it is possible to analyse the correlation between L_{prog} and M_{Ni} with new and improved data. A few other works have analysed empirically the dependence of SN II observables on initial mass computed from L_{prog} (e.g. [Smartt et al. 2009](#); [Otsuka et al. 2012](#); [Maguire et al. 2012](#); [Poznanski 2013](#)). In particular, [Poznanski \(2013\)](#) suggested a correlation between M_i and expansion velocity of the photosphere at 50 d since explosion ($v_{50\text{d}}$). Because of the correlation between $v_{50\text{d}}$ and the absolute V-band magnitude at 50 d since explosion ($M_V^{50\text{d}}$) observed for SNe II ([Hamuy 2003](#)), the relation suggested by [Poznanski \(2013\)](#) could translate into a correlation between L_{prog} and $M_V^{50\text{d}}$. On the theoretical side, the relation between $L_{[\text{O I}]}$ and M_i shown by the nebular spectra models of [Dessart et al. \(2021\)](#) suggests a possible correlation between L_{prog} and $L_{[\text{O I}]}^{350\text{d}}$.

In this work, I investigate empirical correlations between L_{prog} and three SN observables: $L_{[\text{O I}]}^{350\text{d}}$, M_{Ni} , and $M_V^{50\text{d}}$. I use these correlations to compute L_{prog} values for 112 SNe II collected from the literature. The aim is to construct the luminosity distribution for SN II progenitors and compare it to observed RSG luminosity distributions.

The paper is organized as follows. In Section 2, I outline the relevant information on the data used in this study. In Section 3, I present methods to measure $L_{[\text{O I}]}^{350\text{d}}$, L_{prog} from pre-explosion photometry, and to correct the SN sample for selection bias. In Section 4, I report the correlations between L_{prog} and SN observables, the progenitor luminosity distribution, and the comparison with different RSG luminosity distributions. Comparison to previous work and discussion of systematics appear in Section 5. Conclusions are summarised in Section 6.

2 DATA SET

2.1 SN sample

In this work I use the sample of 110 SNe II analysed in [Rodríguez et al. \(2021\)](#). In that work, the authors collected SNe II from the literature having photometry in the radioactive tail in at least one optical band (V , r , R , i , or I) with at least three photometric epochs between 95 and 320 d since explosion. [Rodríguez et al. \(2021\)](#) used these data to compute accurate ^{56}Ni masses for the selected SNe. The authors

² [Dwarkadas \(2014\)](#) reported a similar upper limit of $\sim 19 M_{\odot}$ based on the lack of SNe II with mass-loss rate $> 10^{-5} M_{\odot} \text{ yr}^{-1}$.

also calculated distance moduli (μ), explosion epochs (t_{expl}), host galaxy reddenings (E_{B-V}^{host}), $M_V^{50\text{d}}$ values, and absolute R -band magnitudes at maximum (M_R^{max}), which are used to perform the correction for selection bias; see Section 3.3). Since the six quantities mentioned above were computed in an homogeneous way, the data presented in Rodríguez et al. (2021) are suitable to carry out the present study. I also include SN 2018aoq, for which a progenitor candidate has been identified (O’Neill et al. 2019), and SN 2015bs, which shows a prominent [O I] doublet in its nebular spectrum (Anderson et al. 2018). For these two SNe, I compute μ , t_{expl} , E_{B-V}^{host} , $M_V^{50\text{d}}$, M_R^{max} , and ^{56}Ni mass in the same manner as in Rodríguez et al. (2021) (see Appendix A). The final sample of 112 SNe is listed in Table 1. This includes the SN name (Column 1), the ^{56}Ni mass (Column 2), $M_V^{50\text{d}}$ (Column 3), and M_R^{max} (Column 4).

Among the SNe used in this work, 44 have nebular spectra (1) between 190 and 410 d since explosion; (2) being covered by photometry in at least one of these filters: Johnson-Kron-Cousins VRI or Sloan ri ; and (3) with a wavelength coverage enough to compute synthetic magnitudes for the photometric filters mentioned above. For these SNe, their nebular spectra and photometry are useful to estimate $L_{[\text{O I}]}^{350\text{d}}$. The sample of 44 SNe II is listed in Table 2, which includes the SN name (Column 1), the heliocentric redshift z (Column 2), t_{expl} (Column 3), μ (Column 4), the Galactic reddening E_{B-V}^{MW} (Column 5), E_{B-V}^{host} (Column 6), the number of selected spectra N_{spec} (Column 7), and references for spectroscopic data (Columns 8). Heliocentric redshifts and Galactic reddenings are taken from Rodríguez et al. (2021), while for SN 2015bs I adopt $z = 0.027$ (Anderson et al. 2018) and $E_{B-V}^{\text{MW}} = 0.044 \pm 0.007$ (Schlafly & Finkbeiner 2011). The photometry I use is the same as that used in Rodríguez et al. (2021), while for SN 2015bs I use the photometry of Anderson et al. (2018).

As in Rodríguez et al. (2021), for our Galaxy and host galaxies I assume the extinction curve $R_\lambda = A_\lambda/E_{B-V}$ of Fitzpatrick (1999) with $R_V = A_V/E_{B-V}$ of 3.1, while for SN 2002hh I adopt a host galaxy R_V of 1.1.

2.2 Progenitor sample

Twelve SNe in my sample have photometry of their confirmed or candidate progenitors.³ Difference images between pre-explosion and late-time images, and the corresponding progenitor photometry (in Vega magnitudes) are available for SNe 2003gd, 2004et, 2004A, 2005cs, 2006my, 2008bk, and 2012aw. The progenitor candidates for SNe 2012A, 2012ec, 2013ej, 2017eaw, and 2018aoq are still not confirmed by their disappearance in late-time images, so the reported progenitor photometry is not definitive. For completeness, I include six SNe II for which 3σ detection limits for their progenitors are available: SNe 1999em, 2002hh (5σ detection limit), 2006ov,

Table 1. SN sample.

SN	$\log(M_{\text{Ni}}/M_\odot)$	$M_V^{50\text{d}}$	M_R^{max}
1980K	-1.462(147)	-17.348(379)	-18.764
1986I	-1.302(198)	-16.911(590)	-16.730
1988A	-1.109(185)	-16.488(488)	-16.639
1990E	-1.383(123)	-16.702(341)	-17.401
1990K	-1.470(118)	-16.705(275)	-17.784
1991G	-1.778(99)	-15.365(277)	-15.729
1991al	-1.629(68)	-15.974(159)	-16.836
1992H	-0.788(178)	-17.670(413)	-18.067
1992ba	-1.744(126)	-15.733(305)	-16.218
1994N	-2.283(106)	-14.955(233)	-15.371
1995ad	-1.230(115)	-17.086(387)	-17.782
1996W	-0.952(97)	-17.469(256)	-17.798
1997D	-2.064(144)	< -14.436(423)	-14.986
1999ca	-1.846(70)	-16.804(167)	-18.086
1999em	-1.296(62)	-16.692(138)	-17.192
1999ga	-1.446(120)	< -16.693(285)	-17.320
1999gi	-1.333(87)	-16.250(207)	-16.728
2001X	-1.395(97)	-16.348(231)	-16.726
2001dc	-2.119(110)	-15.059(283)	-15.283
2002gw	-1.631(103)	-16.017(246)	-16.310
2002hh	-1.082(69)	-16.882(285)	-17.107
2002hx	-1.186(64)	-16.671(165)	-17.596
2003B	-2.223(115)	-14.768(271)	-15.248
2003T	-1.344(101)	-16.674(164)	-17.131
2003Z	-2.262(116)	-14.610(277)	-14.958
2003fb	-1.482(111)	-16.016(206)	-16.582
2003gd	-1.694(99)	< -16.405(149)	-16.859
2003hd	-1.362(63)	-17.056(156)	-17.635
2003hk	-1.572(105)	-17.101(211)	-18.303
2003hn	-1.412(56)	-16.819(136)	-17.602
2003ho	-1.601(105)	-16.554(267)	-17.415
2003iq	-1.318(82)	-16.763(200)	-17.347
2004A	-1.604(116)	-15.898(291)	-16.159
2004dj	-1.902(130)	-15.846(178)	-16.232
2004eg	-2.126(188)	< -15.077(551)	-15.693
2004ej	-1.793(166)	-16.494(380)	-17.026
2004et	-1.037(71)	-17.645(213)	-17.974
2004fx	-1.802(173)	-15.720(400)	-15.984
2005af	-1.477(179)	< -15.212(383)	-17.413
2005au	-1.195(85)	-17.291(273)	-17.974
2005ay	-1.778(109)	-15.512(239)	-15.912
2005cs	-2.241(76)	-15.371(133)	-15.700
2005dx	-2.064(194)	-15.583(445)	-16.381
2006my	-1.674(141)	< -15.361(473)	-16.896
2006ov	-2.051(267)	< -16.568(707)	-16.195
2007aa	-1.522(143)	-16.556(407)	-16.703
2007hv	-1.326(125)	-16.698(400)	-17.158
2007it	-0.987(130)	-17.400(417)	-18.234
2007od	-	-17.438(332)	-18.027
2008K	-1.611(180)	-16.806(378)	-17.869
2008M	-1.605(172)	-16.504(396)	-17.236
2008aw	-1.074(114)	-17.228(230)	-18.181
2008bk	-2.064(94)	-14.992(366)	-15.245
2008gz	-1.253(81)	< -16.366(194)	-17.679
2008in	-1.640(258)	-16.134(644)	-16.596
2009N	-1.891(161)	-15.357(404)	-15.609
2009at	-1.750(115)	-16.153(332)	-17.283
2009ay	-0.932(116)	-17.720(309)	-18.552
2009bw	-1.737(120)	-16.393(316)	-17.309
2009dd	-1.474(112)	-16.385(259)	-16.993
2009hd	-1.959(66)	-16.632(188)	-17.327
2009ib	-1.356(75)	-15.790(131)	-16.266
2009md	-2.097(78)	-15.365(195)	-15.779
2010aj	-2.088(75)	-16.764(203)	-17.836

³ I do not include SN 2009md because the source identified as its progenitor by Fraser et al. (2011) is still present in images taken three years after the SN explosion (Maud et al. 2015).

Table 1 – *continued*

SN	$\log(M_{\text{Ni}}/M_{\odot})$	$M_V^{50\text{d}}$	M_R^{max}
PTF10gva	-1.111(138)	–	-18.794
2011fd	-1.498(125)	–	-16.998
PTF11go	-1.593(160)	–	-16.743
PTF11htj	-1.309(175)	–	-16.946
PTF11lzt	-1.651(159)	–	-16.348
2012A	-1.766(111)	-16.454(284)	-17.176
2012aw	-1.269(55)	-16.847(135)	-17.181
2012br	-1.219(254)	–	-17.764
2012cd	-1.038(168)	–	-18.680
2012ec	-1.545(115)	-16.336(290)	-16.695
PTF12grj	-1.565(169)	–	-16.963
PTF12hsx	-1.090(225)	–	-17.331
2013K	-1.593(123)	-16.711(297)	-16.430
2013ab	-1.482(95)	-16.199(234)	-16.804
2013am	-1.695(163)	-15.470(358)	-15.958
2013bu	-1.888(93)	-16.104(217)	-16.947
2013by	-1.512(151)	-17.397(436)	-18.411
2013ej	-1.551(60)	-16.950(149)	-17.900
2013fs	-1.323(106)	-16.739(213)	-17.623
2013hj	-1.092(73)	-17.564(178)	-18.270
iPTF13dkz	-1.173(205)	–	-16.470
LSQ13dpa	-1.101(135)	-17.181(470)	-17.694
2014G	-1.146(77)	-17.203(199)	-18.411
2014cx	-1.251(103)	-16.668(263)	-16.957
2014cy	-1.820(117)	-15.584(269)	-16.122
ASASSN-14dq	-1.308(101)	-16.967(249)	-17.653
2014dw	-1.544(158)	-16.238(487)	-17.312
ASASSN-14ha	-2.030(120)	-15.963(369)	-16.379
OGLE14-18	-1.367(123)	–	-17.103
2015V	-1.643(107)	-15.751(287)	-15.970
2015W	-1.372(110)	-17.129(314)	-17.893
2015an	-1.575(113)	-17.184(363)	-17.697
2015ba	-1.840(114)	-17.020(221)	-17.750
2015bs	-1.156(119)	-16.988(325)	-17.470
2015cz	-1.344(93)	-17.158(272)	-17.627
ASASSN-15oz	-0.875(124)	-17.682(316)	-18.478
2016X	-1.349(147)	-16.856(371)	-17.588
2016aqf	-1.670(137)	-16.024(394)	-16.136
2016bkv	-1.817(106)	-14.537(300)	-15.741
2016gfy	-1.122(103)	-17.145(263)	-17.599
2016ija	-1.582(144)	-16.691(490)	-17.238
2017it	-1.257(60)	-16.817(149)	-17.178
2017ahn	-1.316(132)	-16.751(464)	-18.286
2017eaw	-1.087(69)	-17.265(203)	-17.828
2017gmr	-0.857(93)	-17.655(235)	-18.005
2018aoq	-2.022(58)	-15.613(136)	-16.029
2018cuf	-1.417(121)	-16.898(359)	-17.224
2018hwm	-2.205(124)	-15.041(284)	-15.191

Note. Numbers in parentheses are 1σ errors in units of 0.001.

2007aa, 2009hd,⁴ and 2009ib.⁵ The list of the 18 SNe II with progenitor photometry or upper limits is summarized in Table 3. This includes the SN name (Column 1), μ (Column 2), E_{B-V}^{MW} (Column 3), E_{B-V}^{host} (Column 4), the filter used to observe the progenitor (x), the apparent progenitor magnitude

⁴ As in Smartt (2015), I adopt the progenitor magnitude of SN 2009hd as an upper limit because it is close to the 3σ detection limit (see Elias-Rosa et al. 2011).

⁵ I assume the scenario where the progenitor is not the yellow source detected at the SN position but a RSG too faint to be detected (see Takáts et al. 2015).

($m_{\text{prog},x}$), and its reference (Columns 5, 6, and 7, respectively).

2.3 RSG samples

For the comparison between luminosities of SN II progenitors and RSGs, I use the RSG samples reported by Neugent et al. (2020) for LMC, by Massey et al. (2021b) for SMC, and by Massey et al. (2021a) for M31 and M33. The authors used JK_S photometry to identify RSGs in the colour-magnitude diagram and to compute luminosities using the BC technique. The RSG samples of LMC, M31, and M33 (SMC) are complete to a luminosity limit of $\log(L/L_{\odot}) = 4.0$ dex (3.7 dex). For this work, I re-compute RSG luminosities using the most recent and precise distances reported for the galaxies mentioned above. For LMC and SMC I adopt distance moduli of 18.477 ± 0.024 (Pietrzyński et al. 2019) and 18.977 ± 0.032 mag (Graczyk et al. 2020), respectively, which are based on late-type eclipsing binary stars. For M31 and M33 I adopt distance moduli of 24.407 ± 0.032 (Li et al. 2021) and 24.568 ± 0.064 mag (Zgirski et al. 2021), respectively, estimated using the near-infrared Cepheid period-luminosity relation and the J -region Asymptotic Giant Branch method, respectively. As Massey et al. (2021a) mentioned, the M31 sample includes stars with unlikely large extinction values and therefore unrealistic high luminosities. In order not to include those stars in the analysis, I remove stars with $A_V \geq 2.5$ mag (around 0.4 per cent of the total sample).

3 METHODOLOGY

3.1 [O I] $\lambda\lambda 6300, 6364$ line luminosity

To compute $L_{[\text{O I}]}$, it is necessary to calibrate the flux of the spectra in the wavelength region of the [O I] doublet. For this, I scale each spectrum by a constant C such that $\log C = 0.4(m_{x,\text{syn}} - m_{x,t_{\text{spec}}})$. Here, $m_{x,\text{syn}}$ is the x -band synthetic magnitude computed from the spectrum, $m_{x,t_{\text{spec}}}$ is the SN apparent magnitude at the epoch of the spectrum (t_{spec}), and angle brackets denote an average over the bands used to estimate C . To compute synthetic magnitudes I use the methodology of Rodríguez et al. (2021), while to interpolate photometry to the epochs of the spectra I use the ALR code⁶ (Rodríguez et al. 2019). This code performs `loess` non-parametric regressions (Cleveland et al. 1992) to the input data, taking into account observed and intrinsic errors, along with the presence of possible outliers. For the flux calibration of the spectra, I use V and r/R photometry. If it is not possible to calculate $m_{x,\text{syn}} - m_{x,t}$ for one of those bands, then the i/I band is included. In the case of SN 2015bs, I extrapolate its R -band photometry (see Appendix A) to the epoch of the spectrum using a straight line fit.

Once the flux of each spectrum is calibrated, the flux of the [O I] $\lambda\lambda 6300, 6364$ line is given by

$$F_{[\text{O I}]} = h \sum_{i=1}^n (f_i - f_{c,\lambda_i}). \quad (1)$$

Here, f_i and f_{c,λ_i} are the observed and continuum flux at

⁶ <https://github.com/olrodrig/ALR>

Table 2. Sample of SNe with useful nebular spectroscopy.

SN	cz (km s ⁻¹)	t_{expl} (MJD)	μ (mag)	E_{B-V}^{MW} (mag)	E_{B-V}^{host} (mag)	N_{spec}	References [†]
1990E	1362	47934.4 ± 1.4	30.83 ± 0.26	0.022 ± 0.003	0.598 ± 0.072	7	1, 2, 3
1990K	1584	48013.8 ± 4.2	31.57 ± 0.24	0.012 ± 0.002	0.227 ± 0.034	2	4, 5
1991G	757	48281.5 ± 5.3	30.76 ± 0.17	0.017 ± 0.003	0.025 ± 0.071	1	6
1992H	1793	48656.4 ± 4.5	32.07 ± 0.17	0.015 ± 0.002	0.167 ± 0.123	6	5, 7, 8
1994N	2940	49453.9 ± 4.5	33.24 ± 0.20	0.032 ± 0.005	0.045 ± 0.036	1	9
1996W	1617	50180.2 ± 2.5	31.86 ± 0.19	0.036 ± 0.006	0.260 ± 0.054	3	10
1997D	1217	50361.0 ± 15.0	30.93 ± 0.25	0.017 ± 0.003	0.090 ± 0.111	1	11
1999em	800	51474.5 ± 2.0	30.31 ± 0.09	0.035 ± 0.006	0.082 ± 0.034	4	12, 13
1999ga	1466	51419.5 ± 20.0	31.51 ± 0.05	0.173 ± 0.028	0.511 ± 0.084	1	14
2002hh	110	52575.6 ± 2.5	29.44 ± 0.09	1.065 ± 0.046	1.545 ± 0.182	2	15, 16
2003B	1141	52622.2 ± 4.2	30.62 ± 0.25	0.023 ± 0.004	0.023 ± 0.033	1	17
2003gd	657	52716.5 ± 21.0	29.95 ± 0.08	0.060 ± 0.010	0.144 ± 0.040	1	16
2004A	852	53012.5 ± 1.7	30.87 ± 0.26	0.013 ± 0.002	0.177 ± 0.043	1	5
2004dj	221	53180.6 ± 15.6	27.46 ± 0.11	0.034 ± 0.006	0.094 ± 0.035	7	5, 18
2004et	40	53270.5 ± 0.3	29.44 ± 0.09	0.293 ± 0.047	0.073 ± 0.043	20	16, 19, 20
2005ay	850	53450.7 ± 1.8	30.68 ± 0.21	0.018 ± 0.003	0.035 ± 0.037	1	16
2005cs	463	53548.4 ± 0.3	29.67 ± 0.07	0.032 ± 0.005	0.124 ± 0.037	6	16, 21
2006my	788	53942.5 ± 20.0	31.40 ± 0.10	0.012 ± 0.002	-0.062 ± 0.152	4	5, 20
2006ov	1566	53973.5 ± 6.0	31.40 ± 0.63	0.019 ± 0.003	0.275 ± 0.105	1	22
2007it	1193	54348.0 ± 0.6	30.56 ± 0.24	0.099 ± 0.016	0.109 ± 0.111	6	17
2008bk	230	54547.1 ± 2.6	27.66 ± 0.08	0.017 ± 0.003	0.090 ± 0.111	4	17
2008gz	1862	54693.5 ± 5.0	32.22 ± 0.15	0.036 ± 0.006	-0.031 ± 0.040	1	23
2009N	905	54850.1 ± 3.4	30.90 ± 0.38	0.018 ± 0.003	0.265 ± 0.045	2	24
2009dd	757	54916.0 ± 4.2	30.76 ± 0.17	0.017 ± 0.003	0.285 ± 0.057	2	10
2009ib	1304	55040.3 ± 4.0	31.41 ± 0.05	0.026 ± 0.004	0.147 ± 0.038	2	25
2011fd	2101	55777.9 ± 4.5	32.41 ± 0.22	0.063 ± 0.010	0.090 ± 0.111	1	5
2012A	753	55929.3 ± 2.6	30.66 ± 0.24	0.027 ± 0.004	0.040 ± 0.049	1	5
2012aw	778	56002.0 ± 0.5	29.93 ± 0.05	0.024 ± 0.004	0.115 ± 0.041	6	5, 26, 27
2012ec	1407	56144.5 ± 3.4	31.07 ± 0.25	0.023 ± 0.004	0.102 ± 0.048	2	5, 28
2013K	2418	56294.5 ± 4.2	32.48 ± 0.21	0.122 ± 0.019	0.512 ± 0.066	1	29
2013am	1114	56371.8 ± 0.4	30.36 ± 0.29	0.021 ± 0.003	0.536 ± 0.069	1	5
2013by	1144	56401.6 ± 3.6	30.46 ± 0.29	0.188 ± 0.030	0.196 ± 0.100	1	30
2013ej	657	56496.8 ± 0.2	29.95 ± 0.08	0.060 ± 0.010	0.044 ± 0.040	3	31, 32
2014G	1160	56669.3 ± 0.8	31.96 ± 0.14	0.010 ± 0.002	0.268 ± 0.046	1	33
2014cx	1646	56901.9 ± 0.3	31.51 ± 0.22	0.096 ± 0.015	-0.021 ± 0.045	2	34
ASASSN-14ha	1504	56909.5 ± 0.6	30.86 ± 0.15	0.008 ± 0.001	0.090 ± 0.111	1	35
2015ba	2383	57347.5 ± 4.9	32.80 ± 0.16	0.015 ± 0.002	0.416 ± 0.047	1	36
2015bs	8100	56921.5 ± 2.6	35.10 ± 0.11	0.044 ± 0.007	0.000 ± 0.100	1	37
ASASSN-15oz	2078	57259.1 ± 1.9	31.90 ± 0.26	0.078 ± 0.013	0.230 ± 0.056	3	38
2016aqf	1204	57442.6 ± 0.3	31.01 ± 0.25	0.047 ± 0.008	0.180 ± 0.100	5	39
2016gfy	2416	57641.3 ± 2.6	32.64 ± 0.22	0.086 ± 0.014	0.163 ± 0.045	2	40
2017eaw	40	57886.2 ± 0.6	29.44 ± 0.09	0.293 ± 0.047	0.059 ± 0.037	4	41
2018cuf	3248	58291.8 ± 0.3	33.10 ± 0.19	0.028 ± 0.004	0.221 ± 0.100	1	42
2018hwm	2684	58424.8 ± 0.9	33.08 ± 0.19	0.022 ± 0.004	0.150 ± 0.069	1	43

Note. Quoted uncertainties are 1 σ errors.

[†](1) Schmidt et al. (1993); (2) Benetti et al. (1994); (3) Gómez & López (2000); (4) Cappellaro et al. (1995); (5) Silverman et al. (2017); (6) Blanton et al. (1995); (7) Clocchiatti et al. (1996); (8) Filippenko (1997); (9) Pastorello et al. (2004); (10) Inserra et al. (2013); (11) Benetti et al. (2001); (12) Leonard et al. (2002); (13) Elmhamdi et al. (2003); (14) Pastorello et al. (2009b); (15) Mattila et al. (2004); (16) Faran et al. (2014); (17) Gutiérrez et al. (2017); (18) Leonard et al. (2006); (19) Sahu et al. (2006); (20) Maguire et al. (2010); (21) Pastorello et al. (2009a); (22) Spiro et al. (2014); (23) Roy et al. (2011); (24) Takáts et al. (2014); (25) Takáts et al. (2015); (26) Bose et al. (2013); (27) Jerkstrand et al. (2014); (28) Jerkstrand et al. (2015); (29) Tomasella et al. (2018); (30) Black et al. (2017); (31) Yuan et al. (2016); (32) Berkeley SuperNova Database (SNDB; Silverman et al. 2012); (33) Terreran et al. (2016); (34) Huang et al. (2016); (35) Public ESO Spectroscopic Survey for Transient Objects Survey (PESSTO; Smartt et al. 2015); (36) Dastidar et al. (2018); (37) Anderson et al. (2018); (38) Bostroem et al. (2019); (39) Müller-Bravo et al. (2020); (40) Singh et al. (2019); (41) Van Dyk et al. (2019); (42) Dong et al. (2020); (43) Reguitti et al. (2021).

wavelength λ_i , respectively, h is the spectral dispersion, and n is the number of pixels between the blue and red endpoints of the [O I] doublet (λ_1 and λ_n , respectively).

To estimate the flux of the continuum, I fit the [O I] doublet with a double Gaussian separated by 6.4 nm plus a straight line corresponding to $f_{c,\lambda}$ (e.g. Elmhamdi 2011). Fig. 1 shows this analytical fit applied to the [O I] doublet of SN 2009N at

370 d since the explosion. I adopt as λ_1 and λ_n the wavelengths for which the extremes of the double Gaussian are equal to one per cent of the maximum.

The error on $\log F_{[\text{O I}]}$ is given by

$$\sigma_{\log F_{[\text{O I}]}} = \sqrt{\left[\frac{h}{\ln(10)F_{[\text{O I}]}}\right]^2 \sum_{i=1}^n (\sigma_{f_i}^2 + \sigma_{f_{c,\lambda_i}}^2) + \frac{\sigma_m^2}{6.25}}, \quad (2)$$

Table 3. SN II progenitor sample

SN	μ	E_{B-V}^{MW}	E_{B-V}^{host}	x	$m_{\text{prog},x}$	Reference
1999em	30.31 ± 0.09	0.035 ± 0.006	0.082 ± 0.034	I	>23.0	Smartt et al. (2009)
2002hh	29.44 ± 0.09	1.065 ± 0.046	1.545 ± 0.182	i'_{Gunn}	>22.8	Smartt et al. (2009)
2003gd	29.95 ± 0.08	0.060 ± 0.010	0.144 ± 0.040	I_J	23.14 ± 0.08	Maund & Smartt (2009)
2004A	30.87 ± 0.26	0.013 ± 0.002	0.177 ± 0.043	WFPC2 F814W	24.36 ± 0.12	Maund et al. (2014a)
2004et	29.44 ± 0.09	0.293 ± 0.047	0.073 ± 0.043	I_J	21.88 ± 0.17	Crockett et al. (2011)
2005cs	29.67 ± 0.07	0.032 ± 0.005	0.124 ± 0.037	ACS/WFC F814W	23.62 ± 0.07	Maund et al. (2014a)
2006my	31.40 ± 0.10	0.012 ± 0.002	-0.062 ± 0.152	WFPC2 F814W	24.86 ± 0.13	Maund et al. (2014a)
2006ov	31.40 ± 0.63	0.019 ± 0.003	0.275 ± 0.105	WFPC2 F814W	>24.2	Crockett et al. (2011)
2007aa	31.99 ± 0.27	0.023 ± 0.004	0.046 ± 0.100	WFPC2 F814W	>24.44	Smartt et al. (2009)
2008bk	27.66 ± 0.08	0.017 ± 0.003	0.090 ± 0.111	K_S	18.39 ± 0.03	Maund et al. (2014b)
2009hd	30.15 ± 0.07	0.029 ± 0.005	1.206 ± 0.056	WFPC2 F814W	>23.54	Elias-Rosa et al. (2011)
2009ib	31.41 ± 0.05	0.026 ± 0.004	0.147 ± 0.038	WFPC2 F814W	>23.25	Takáts et al. (2015)
2012A	30.66 ± 0.24	0.027 ± 0.004	0.040 ± 0.049	K'	20.29 ± 0.13	Tomasella et al. (2013)
2012aw	29.93 ± 0.05	0.024 ± 0.004	0.115 ± 0.041	K_S	19.56 ± 0.29	Fraser (2016)
2012ec	31.07 ± 0.25	0.023 ± 0.004	0.102 ± 0.048	WFPC2 F814W	23.39 ± 0.18	Maund et al. (2013)
2013ej	29.95 ± 0.08	0.060 ± 0.010	0.044 ± 0.040	ACS/WFC F814W	22.66 ± 0.03	Fraser et al. (2014)
2017eaw	29.44 ± 0.09	0.293 ± 0.047	0.059 ± 0.037	WFC3/IR F160W	19.36 ± 0.01	Van Dyk et al. (2019)
2018aoq	30.99 ± 0.06	0.023 ± 0.004	0.086 ± 0.040	WFC3/IR F160W	21.84 ± 0.05	O'Neill et al. (2019)

Note. Quoted uncertainties are 1σ errors.

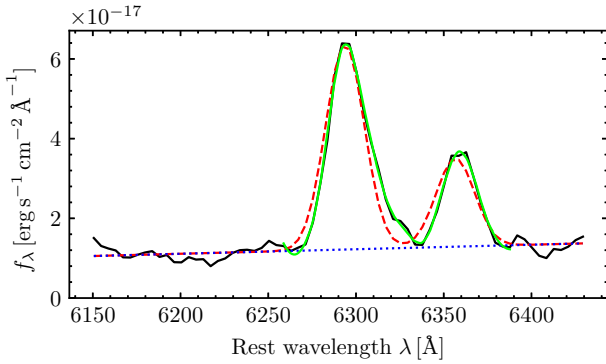


Figure 1. Spectrum of SN 2009N at 370 d since explosion showing the [O I] $\lambda\lambda 6300, 6364$ line. The red dashed line is the double Gaussian fit plus a straight line (blue dotted line), while the green solid line corresponds to the ALR fit.

where σ_{f_i} and $\sigma_{f_{c,\lambda_i}}$ are the errors on f_i and f_{c,λ_i} , respectively, and σ_m is the mean error of the photometry used to calibrate the spectrum. To estimate σ_{f_i} , I fit the [O I] doublet with the ALR code, and then assume the sample standard deviation ($\hat{\sigma}$) around the ALR fit as the error on σ_{f_i} . I also assume $\sigma_{f_{c,\lambda_i}} = \sigma_{f_i}$.

The luminosity of the [O I] doublet (in units of erg s^{-1}) is given by

$$\log L_{[\text{O I}]} = \log F_{[\text{O I}]} + (\mu + R_{6332} E_{B-V}) / 2.5 + 40.078, \quad (3)$$

where $F_{[\text{O I}]}$ is in units of $\text{erg s}^{-1} \text{cm}^{-2}$, E_{B-V} is the total reddening, $R_{6332} = 2.49$ is the R_λ value at $\lambda = 6332 \text{ \AA}$ (the middle wavelength of the [O I] doublet),⁷ and the constant term provides the conversion from magnitude to cgs units. The $\log L_{[\text{O I}]}$ values are shown in the top panel of Fig. 2 against time since explosion $t = (t_{\text{spec}} - t_{\text{expl}}) / (1 + z)$.

To calculate $\log L_{[\text{O I}]}^{350\text{d}}$, I construct an analytical expression

⁷ In the case of SN 2002hh, the term $R_{6332} E_{B-V}$ is replaced by $2.49 E_{B-V}^{\text{MW}} + R_{6332} E_{B-V}^{\text{host}}$, where $R_{6332} = 0.53$ for $R_V = 1.1$.

for $\log L_{[\text{O I}]}$ as a function of t , $\log L_{[\text{O I}]}(t)$, which is then evaluated at $t = 350$ d. For each SN, I model $\log L_{[\text{O I}]}(t)$ as

$$\log L_{[\text{O I}]}(t) = \delta + \Psi(t), \quad (4)$$

where δ is the vertical intercept of $\log L_{[\text{O I}]}(t)$, and $\Psi(t)$ is a polynomial representing the dependence of $\log L_{[\text{O I}]}(t)$ on t (i.e. the shape of the curve). Under the assumption that the $\log L_{[\text{O I}]}(t)$ curves of all SNe II have the same shape, the parameters of $\Psi(t)$ can be computed minimizing

$$s^2 = \sum_{j=1}^{N_{\text{SNe}}} \sum_{i=1}^{N_{\text{spec},j}} [\log L_{[\text{O I}]}(t_{j,i}) - a_j - \Psi(t_{j,i})]^2. \quad (5)$$

Here, N_{SNe} is the number of SNe, a_j is an additive term to normalize the $\log L_{[\text{O I}]}$ values of each SN to the same scale, while the polynomial order of $\Psi(t)$ is determined with the Bayesian information criterion (Schwarz 1978). To estimate $\Psi(t)$, I use 17 SNe having two or more $\log L_{[\text{O I}]}$ measurements covering a time range of at least 40 d.

The bottom panel of Fig. 2 shows the result of the minimization of equation (5). I find that $\Psi(t)$ is quadratic on t , given by

$$\Psi(t) = 0.670 \left(\frac{t}{100 \text{ d}} \right) - 0.154 \left(\frac{t}{100 \text{ d}} \right)^2, \quad (6)$$

with $\hat{\sigma} = 0.068$ dex. Once the shape of $\log L_{[\text{O I}]}(t)$ is known, the δ value for each SN can be computed using the weighted mean

$$\delta = \frac{\sum_{i=1}^{N_{\text{spec}}} (w_i \cdot [\log L_{[\text{O I}]}(t_i) - \Psi(t_i)])}{\sum_{i=1}^{N_{\text{spec}}} w_i}, \quad (7)$$

with weights $w_i = 1 / (\sigma_{\log F_{[\text{O I}]}(t_i)}^2 + \hat{\sigma}^2)$. The error on δ is given by the weighted mean error.

I compute $\log L_{[\text{O I}]}^{350\text{d}}$ using equations (4) and (6), and the corresponding δ value. Those estimates are listed in Table 4 along with their errors, given by

$$\sigma_{\log L_{[\text{O I}]}^{350\text{d}}} = \sqrt{\sigma_\delta^2 + \frac{\sigma_\mu^2 + R_{6332}^2 \sigma_{E_{B-V}}^2}{6.25} + 0.412 \left[\frac{\sigma_{t_{\text{expl}}}}{100 \text{ d}} \right]^2}. \quad (8)$$

The mean $\log L_{[\text{O I}]}^{350\text{d}}$ error is of 0.13 dex, of which 65 per cent is induced by errors on distance and host galaxy reddening.

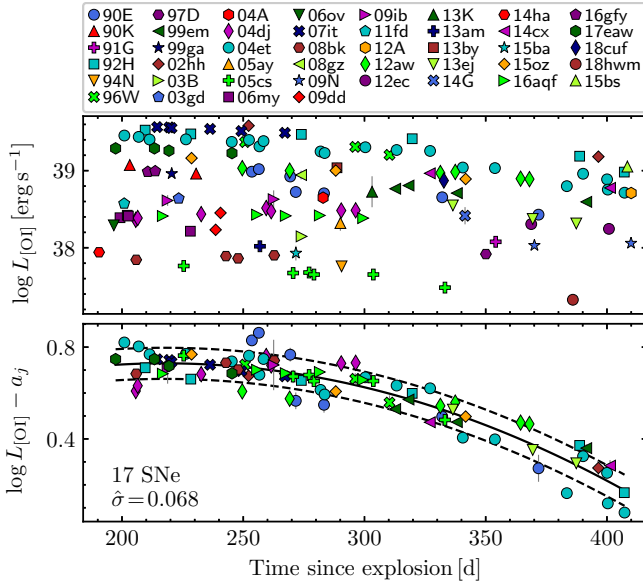


Figure 2. Top panel: [O I] $\lambda\lambda 6300, 6364$ line luminosity as a function of time since explosion. Bottom panel: $\log L_{[\text{O I}]} - a_j$ against time since explosion for the 17 SNe used to estimate $\Psi(t)$. The solid line is a quadratic fit corresponding to $\Psi(t)$, while dashed lines are $\pm 1\sigma$ limits.

Table 4. [O I] $\lambda\lambda 6300, 6364$ line luminosities at 350 d.

SN	$\log L_{[\text{O I}]}^{350\text{d}}$	SN	$\log L_{[\text{O I}]}^{350\text{d}}$
1990E	38.627 ± 0.130	2009N	38.241 ± 0.167
1990K	38.751 ± 0.114	2009dd	38.085 ± 0.105
1991G	38.095 ± 0.137	2009ib	38.359 ± 0.088
1992H	39.276 ± 0.144	2011fd	38.308 ± 0.161
1994N	37.571 ± 0.125	2012A	39.010 ± 0.131
1996W	39.106 ± 0.103	2012aw	38.885 ± 0.053
1997D	37.919 ± 0.184	2012ec	38.440 ± 0.125
1999em	38.695 ± 0.061	2013K	38.569 ± 0.233
1999ga	38.692 ± 0.141	2013am	37.773 ± 0.153
2002hh	38.926 ± 0.086	2013by	38.845 ± 0.181
2003B	37.927 ± 0.128	2013ej	38.481 ± 0.065
2003gd	38.370 ± 0.121	2014G	38.382 ± 0.144
2004A	38.446 ± 0.132	2014cx	38.950 ± 0.112
2004dj	38.213 ± 0.089	ASASSN-14ha	37.682 ± 0.152
2004et	39.095 ± 0.074	2015ba	37.705 ± 0.138
2005ay	38.131 ± 0.147	2015bs	39.344 ± 0.149
2005cs	37.460 ± 0.055	ASASSN-15oz	38.853 ± 0.126
2006my	38.089 ± 0.180	2016aqf	38.187 ± 0.145
2006ov	38.027 ± 0.284	2016gfy	38.720 ± 0.112
2007it	39.277 ± 0.150	2017eaw	39.000 ± 0.078
2008bk	37.619 ± 0.121	2018cuf	38.805 ± 0.146
2008gz	38.722 ± 0.113	2018hwm	37.492 ± 0.140

Notes. $L_{[\text{O I}]}^{350\text{d}}$ values are in units of erg s^{-1} . Quoted uncertainties are 1σ errors.

3.2 Progenitor luminosity from pre-explosion photometry

For the SNe listed in Table 3, I compute L_{prog} (in units of L_{\odot}) using the BC technique

$$\log L_{\text{prog}} = (\mu - \text{BC}_x - m_{\text{prog},x} + R_{\lambda_x} E_{B-V} + 4.74)/2.5, \quad (9)$$

Table 5. Adopted bolometric corrections.

SN	BC_x	SN	BC_x
1999em	-0.32 ± 0.15	2008bk	3.00 ± 0.18
2002hh	-0.49 ± 0.15	2009hd	0.00 ± 0.15
2003gd	0.60 ± 0.17	2009ib	0.00 ± 0.15
2004A	0.00 ± 0.15	2012A	3.00 ± 0.18
2004et	0.25 ± 0.15	2012aw	3.00 ± 0.18
2005cs	0.05 ± 0.15	2012ec	0.00 ± 0.15
2006my	0.00 ± 0.15	2013ej	0.40 ± 0.20
2006ov	0.00 ± 0.15	2017eaw	2.60 ± 0.10
2007aa	0.00 ± 0.15	2018aoq	2.60 ± 0.10

Note. Quoted uncertainties are 1σ errors.

Table 6. Effective wavelengths and R_{λ_x} values.

x	λ_x (Å)	R_{λ_x}
i'_{Gunn}	7720	1.82^{\dagger}
WFPC2 F814W	8010	1.71
I	8030	1.70
ACS/WFC F814W	8050	1.69
I_J	8640	1.50
WFC3/IR F160W	15290	0.58
K'	21060	0.36
K_S	21520	0.35

$^{\dagger} R_{\lambda_x} = 0.31$ for $R_V = 1.1$.

where BC_x and λ_x are the x -band BC and effective wavelength, respectively.⁸ In this work I use the empirical BCs for RSGs presented in Davies & Beasor (2018, 2020). For 16 of the 18 SN II progenitors listed in Table 3, I adopt the BC_x estimates reported by Davies & Beasor (2018, 2020). For the progenitor of SN 2009ib, I adopt the average BC_{F814W} value for late-type RSGs of 0.00 ± 0.15 computed by Davies & Beasor (2018). For the progenitor of SN 2003gd, identified as a M0 to M2 RSG (Maund & Smartt 2009), I compute a Johnson I -band BC of 0.60 ± 0.17 by averaging the BC_I values for M0-M2 RSGs presented in Fig. 2 of Davies & Beasor (2018). The adopted BC_x values are listed in Table 5.

The x -band effective wavelength is defined as

$$\lambda_x = \frac{\int d\lambda S_{x,\lambda} \lambda^2 f_{\lambda}}{\int d\lambda S_{x,\lambda} \lambda f_{\lambda}} \quad (10)$$

(e.g. Bessell & Murphy 2012), where $S_{x,\lambda}$ is the photon-counting response function for the x -band, and f_{λ} is the SED of the progenitor. To estimate λ_x for the filters listed in Column 5 of Table 3, I use the response functions available in the SVO Filter Profile Service⁹ (Rodrigo et al. 2012; Rodrigo & Solano 2020), and assume a Planck function as f_{λ} , using temperatures between 3400 and 4500 K to represent the SEDs of RSGs. Then, I compute λ_x estimates for 10^4 temperature values randomly selected from a uniform distribution between 3400 and 4500 K, and adopt the mean of these estimates as the final effective wavelength. Table 6 lists the final λ_x values and the corresponding R_{λ_x} estimates for different bands.

The $\log L_{\text{prog}}$ values computed from progenitor photometry ($\log L_{\text{prog}}(\text{phot})$), are listed in Column 2 of Table 7. The

⁸ In the case of SN 2002hh, the term $R_{\lambda_x} E_{B-V}$ is replaced by $R_{\lambda_x} E_{B-V}^{\text{MW}} + R'_{\lambda_x} E_{B-V}^{\text{host}}$, where R'_{λ_x} is the R_{λ_x} value for $R_V = 1.1$.

⁹ <http://svo2.cab.inta-csic.es/theory/fps/>

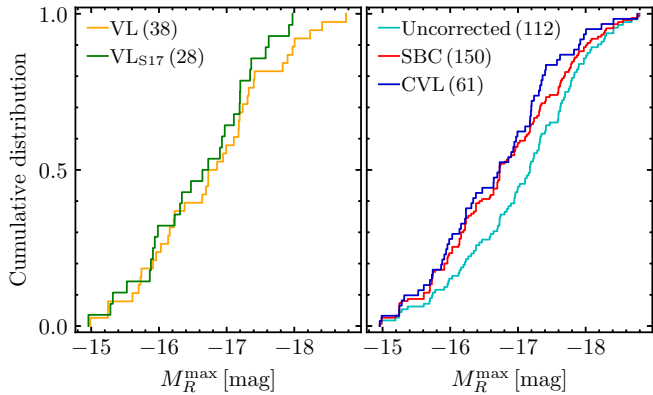


Figure 3. Left-hand panel: cumulative distributions for the M_R^{\max} values in the volume-limited (orange line) and VL_{S17} (green line) samples. Right-hand panel: cumulative M_R^{\max} distributions for the SN sample uncorrected (cyan line) and corrected for selection bias (red line), and for the combined volume-limited sample (blue line). Numbers in parentheses are the sample sizes.

mean $\log L_{\text{prog}}(\text{phot})$ error is of 0.10 dex, of which 46 and 26 per cent is induced by errors on BC_x and μ , respectively.

3.3 Selection bias correction

The SN sample used in this work, like that of [Rodríguez et al. \(2021\)](#), is affected by selection bias. To correct for this bias, I proceed in a similar way as in [Rodríguez et al. \(2021\)](#), where volume-limited samples were used as references to compute the selection bias correction. I select the 38 SNe in my sample with $\mu \leq 31.2$ (hereafter the VL sample) and the 28 SNe II in the sample of [Shivvers et al. \(2017\)](#) with $\mu \leq 32.9$ (the VL_{S17} sample, available in [Rodríguez et al. 2021](#)). The VL_{S17} set has completeness $\gtrsim 95$ per cent, while SNe II with low luminosity or high reddening have completeness ≈ 70 per cent. To compare the VL set with the VL_{S17} sample, I use their M_R^{\max} values. The cumulative M_R^{\max} distributions for the two samples are shown in the left-hand panel of Fig. 3. I use the k -sample Anderson-Darling (AD) test ([Scholz & Stephens 1987](#)) to evaluate whether the M_R^{\max} samples are drawn from a common unspecified distribution (the null hypothesis), obtaining a standardized test statistics (T_{AD}) of -0.73 with a p -value of 0.80. This means that the null hypothesis cannot be rejected at the 80 per cent significance level. Given that the VL_{S17} and the VL samples are likely drawn from a common M_R^{\max} distribution, I combine them into a single data set, which I refer to as the combined volume-limited (CVL) sample.

Correcting the SN sample for selection bias is equivalent to correcting the set of 74 SNe that are not in the VL sample, which I refer to as the non-complete (NC) set. Table 8 lists the number of SNe in four M_R^{\max} bins of width 1 mag (Column 1) for the NC set (Column 2) and the CVL sample (Column 3). The NC sample is almost the same as that of [Rodríguez et al. \(2021\)](#), for which the selection bias correction is practically negligible for $M_R^{\max} < -16.8$ mag. Therefore, I assume that the NC sample is complete at least down to $M_R^{\max} = -16.8$ mag. Under this assumption, I scale the number of SNe in the CVL sample by a factor of 1.83 to match the number of SNe with $M_R^{\max} < -16.8$ in the NC

and CVL samples, and then subtract the number of SNe in the NC sample. The resulting numbers, listed in Column 4, correspond to the selection bias correction. This is practically zero for the two brightest M_R^{\max} bins, and virtually twice the number of SNe in the VL sample with $M_R^{\max} > -16.8$ (see Column 5). Therefore, to correct the SN sample used in this work for selection bias, I include twice the SNe in the VL sample with $M_R^{\max} > -16.8$. Those SNe are marked with a dagger in Table 7. I refer to this sample of 150 SNe as the selection bias corrected (SBC) sample, which is virtually complete except for SNe II with low luminosity or high reddening.

The right-hand panel of Fig. 3 shows the cumulative distributions for the M_R^{\max} values in the sample used in this work, uncorrected and corrected for selection bias. For comparison, I include the distribution for the CVL set, where its similarity to the SBC sample is evident.

3.4 Linear regression

As we will see in the next section, correlations between $\log L_{\text{prog}}$ and the SN observables $\log L_{[\text{O I}]}^{350\text{d}}$, $\log M_{\text{Ni}}$, and $M_V^{50\text{d}}$ can be expressed as linear regressions. Let $\bar{y}(\theta, x)$ be the model that describes the linear correlation between the observables x and y , where θ is a vector containing the free parameters of the model. Given n measurements of x , y , and their 1σ errors (σ_x, σ_y) , I compute θ by maximizing the posterior probability

$$p(\theta|x, y, \sigma_x, \sigma_y) = p(\theta)\mathcal{L}(\theta|x, y, \sigma_x, \sigma_y), \quad (11)$$

where $p(\theta)$ is the prior function (assumed to be uninformative in this work), and $\mathcal{L}(\theta|x, y, \sigma_x, \sigma_y)$ is the likelihood of the linear model, given by

$$\ln \mathcal{L}(\theta|x, y, \sigma_x, \sigma_y) \propto \sum_{i=1}^n \left[\ln V_i + \frac{(y_i - \bar{y}(\theta, x_i))^2}{V_i} \right]. \quad (12)$$

Here, $V_i = \sigma_{y_i}^2 + (\partial\bar{y}/\partial x)^2 \sigma_{x_i}^2 - 2(\partial\bar{y}/\partial x)\sigma_{xy,i} + \sigma_0^2$ is the variance of $y_i - \bar{y}(\theta, x_i)$, where σ_0 is the error not accounted for the errors in x_i and y_i , and

$$\sigma_{xy,i} = \frac{\partial x_i}{\partial \mu} \frac{\partial y_i}{\partial \mu} \sigma_\mu^2 + \frac{\partial x_i}{\partial E_{B-V}} \frac{\partial y_i}{\partial E_{B-V}} \sigma_{E_{B-V}}^2 \quad (13)$$

is the covariance between x_i and y_i . I maximize the posterior probability in equation (11) by means of a Markov Chain Monte Carlo process using the python package `emcee` ([Foreman-Mackey et al. 2013](#)), which also provides the marginalized distributions of the parameters. I adopt the $\hat{\sigma}$ values of those distributions as the 1σ errors of the free parameters.

4 RESULTS

4.1 Progenitor luminosities

4.1.1 Empirical correlations

Fig. 4 shows $\log L_{\text{prog}}$ against $\log L_{[\text{O I}]}^{350\text{d}}$ (top panel), $\log M_{\text{Ni}}$ (middle panel), and $M_V^{50\text{d}}$ (bottom panel). For these pairs of variables I compute absolute Pearson correlation coefficients $|r_p|$ of 0.84, 0.81, and 0.86, respectively, indicating strong linear correlations. The probability of obtaining $|r_p|$ values ≥ 0.84 , 0.81, and 0.86 from random populations of size 11,

Table 7. Progenitor luminosities.

SN	$\log L_{\text{prog}}(\text{phot})$	$\log L_{\text{prog}}(L_{[\text{O I}]^{350\text{d}}})$	$\log L_{\text{prog}}(M_{\text{Ni}})$	$\log L_{\text{prog}}(M_V^{50\text{d}})$	$\log L_{\text{prog}}$
1980K	–	–	4.787 ± 0.099	4.984 ± 0.109	4.787 ± 0.099
1986I [†]	–	–	4.867 ± 0.119	4.879 ± 0.154	4.867 ± 0.119
1988A [†]	–	–	4.964 ± 0.114	4.777 ± 0.132	4.964 ± 0.114
1990E	–	4.792 ± 0.072	4.827 ± 0.090	4.828 ± 0.101	4.792 ± 0.072
1990K	–	4.839 ± 0.068	4.783 ± 0.089	4.829 ± 0.089	4.839 ± 0.068
1991G [†]	–	4.590 ± 0.074	4.628 ± 0.083	4.508 ± 0.090	4.590 ± 0.074
1991al	–	–	4.703 ± 0.074	4.654 ± 0.071	4.654 ± 0.071
1992H	–	5.038 ± 0.076	5.125 ± 0.111	5.061 ± 0.116	5.038 ± 0.076
1992ba [†]	–	–	4.646 ± 0.091	4.596 ± 0.095	4.646 ± 0.091
1994N	–	4.391 ± 0.071	4.375 ± 0.085	4.409 ± 0.082	4.391 ± 0.071
1995ad	–	–	4.904 ± 0.088	4.921 ± 0.111	4.904 ± 0.088
1996W	–	4.973 ± 0.066	5.043 ± 0.082	5.013 ± 0.086	4.973 ± 0.066
1997D [†]	–	4.523 ± 0.088	4.485 ± 0.098	–	4.523 ± 0.088
1999ca	–	–	4.594 ± 0.075	4.853 ± 0.072	4.853 ± 0.072
1999em	$< 5.027 \pm 0.074$	4.817 ± 0.058	4.870 ± 0.073	4.826 ± 0.069	4.817 ± 0.058
1999ga	–	4.816 ± 0.075	4.795 ± 0.089	–	4.816 ± 0.075
1999gi [†]	–	–	4.852 ± 0.079	4.720 ± 0.078	4.720 ± 0.078
2001X	–	–	4.821 ± 0.082	4.744 ± 0.082	4.744 ± 0.082
2001dc	–	–	4.457 ± 0.086	4.434 ± 0.091	4.457 ± 0.086
2002gw	–	–	4.702 ± 0.084	4.664 ± 0.084	4.702 ± 0.084
2002hh	$< 5.715 \pm 0.081$	4.905 ± 0.062	4.978 ± 0.075	4.872 ± 0.091	4.905 ± 0.062
2002hx	–	–	4.926 ± 0.073	4.821 ± 0.072	4.821 ± 0.072
2003B [†]	–	4.526 ± 0.072	4.405 ± 0.088	4.364 ± 0.088	4.526 ± 0.072
2003T	–	–	4.846 ± 0.083	4.822 ± 0.072	4.822 ± 0.072
2003Z	–	–	4.385 ± 0.088	4.326 ± 0.090	4.385 ± 0.088
2003fb	–	–	4.777 ± 0.086	4.664 ± 0.078	4.664 ± 0.078
2003gd	4.502 ± 0.085	4.694 ± 0.070	4.671 ± 0.083	–	4.616 ± 0.054
2003hd	–	–	4.837 ± 0.073	4.913 ± 0.071	4.913 ± 0.071
2003hk	–	–	4.732 ± 0.084	4.924 ± 0.079	4.924 ± 0.079
2003hn	–	–	4.812 ± 0.072	4.857 ± 0.068	4.857 ± 0.068
2003ho	–	–	4.717 ± 0.084	4.793 ± 0.088	4.717 ± 0.084
2003iq	–	–	4.859 ± 0.078	4.843 ± 0.077	4.843 ± 0.077
2004A [†]	4.630 ± 0.133	4.723 ± 0.073	4.716 ± 0.088	4.636 ± 0.092	4.702 ± 0.064
2004dj [†]	–	4.635 ± 0.063	4.566 ± 0.093	4.623 ± 0.074	4.635 ± 0.063
2004eg	–	–	4.454 ± 0.115	–	4.454 ± 0.115
2004ej	–	–	4.621 ± 0.106	4.779 ± 0.109	4.621 ± 0.106
2004et	5.039 ± 0.105	4.969 ± 0.060	5.000 ± 0.075	5.055 ± 0.079	4.986 ± 0.052
2004fx	–	–	4.616 ± 0.109	4.593 ± 0.113	4.616 ± 0.109
2005af	–	–	4.780 ± 0.111	–	4.780 ± 0.111
2005au	–	–	4.921 ± 0.079	4.970 ± 0.089	4.921 ± 0.079
2005ay [†]	–	4.604 ± 0.077	4.628 ± 0.086	4.543 ± 0.083	4.604 ± 0.077
2005cs [†]	4.401 ± 0.076	4.349 ± 0.057	4.396 ± 0.076	4.509 ± 0.068	4.368 ± 0.046
2005dx	–	–	4.485 ± 0.118	4.560 ± 0.122	4.485 ± 0.118
2006my	4.478 ± 0.137	4.588 ± 0.086	4.681 ± 0.097	–	4.557 ± 0.073
2006ov	$< 4.977 \pm 0.269$	4.564 ± 0.120	4.491 ± 0.149	–	4.564 ± 0.120
2007aa	$< 4.963 \pm 0.141$	–	4.757 ± 0.098	4.793 ± 0.115	4.757 ± 0.098
2007hv	–	–	4.855 ± 0.091	4.828 ± 0.113	4.855 ± 0.091
2007it	–	5.038 ± 0.078	5.026 ± 0.093	4.996 ± 0.117	5.038 ± 0.078
2007od	–	–	–	5.005 ± 0.100	5.005 ± 0.100
2008K	–	–	4.712 ± 0.112	4.853 ± 0.109	4.853 ± 0.109
2008M	–	–	4.715 ± 0.109	4.781 ± 0.112	4.715 ± 0.109
2008aw	–	–	4.982 ± 0.087	4.955 ± 0.082	4.955 ± 0.082
2008bk [†]	4.419 ± 0.081	4.410 ± 0.070	4.485 ± 0.081	4.418 ± 0.106	4.414 ± 0.053
2008gz	–	4.828 ± 0.068	4.892 ± 0.078	–	4.828 ± 0.068
2008in	–	–	4.698 ± 0.145	4.692 ± 0.166	4.698 ± 0.145
2009N [†]	–	4.645 ± 0.083	4.572 ± 0.104	4.506 ± 0.114	4.645 ± 0.083
2009at	–	–	4.643 ± 0.088	4.697 ± 0.100	4.643 ± 0.088
2009ay	–	–	5.053 ± 0.088	5.073 ± 0.095	5.053 ± 0.088
2009bw	–	–	4.649 ± 0.089	4.754 ± 0.097	4.649 ± 0.089
2009dd	–	4.586 ± 0.066	4.781 ± 0.087	4.752 ± 0.086	4.586 ± 0.066
2009hd	$< 5.385 \pm 0.095$	–	4.538 ± 0.074	4.812 ± 0.075	4.538 ± 0.074
2009ib	$< 5.278 \pm 0.068$	4.690 ± 0.063	4.840 ± 0.076	4.610 ± 0.068	4.690 ± 0.063
2009md	–	–	4.468 ± 0.077	4.508 ± 0.076	4.508 ± 0.076
2010aj	–	–	4.473 ± 0.076	4.843 ± 0.077	4.473 ± 0.076

Table 7 – *continued*

SN	$\log L_{\text{prog}}(\text{phot})$	$\log L_{\text{prog}}(L_{[\text{O I}]^{350\text{d}}})$	$\log L_{\text{prog}}(M_{\text{Ni}})$	$\log L_{\text{prog}}(M_V^{50\text{d}})$	$\log L_{\text{prog}}$
PTF10gva	–	–	4.963 ± 0.096	–	4.963 ± 0.096
2011fd	–	4.671 ± 0.081	4.769 ± 0.091	–	4.671 ± 0.081
PTF11go	–	–	4.721 ± 0.104	–	4.721 ± 0.104
PTF11htj	–	–	4.864 ± 0.110	–	4.864 ± 0.110
PTF11izt	–	–	4.692 ± 0.104	–	4.692 ± 0.104
2012A	4.854 ± 0.131	4.937 ± 0.073	4.634 ± 0.086	4.769 ± 0.091	4.917 ± 0.064
2012aw	4.863 ± 0.138	4.889 ± 0.057	4.884 ± 0.072	4.863 ± 0.068	4.886 ± 0.052
2012br	–	–	4.909 ± 0.144	–	4.909 ± 0.144
2012cd	–	–	5.000 ± 0.107	–	5.000 ± 0.107
2012ec†	5.053 ± 0.141	4.721 ± 0.071	4.745 ± 0.088	4.741 ± 0.092	4.788 ± 0.063
PTF12grj	–	–	4.735 ± 0.107	–	4.735 ± 0.107
PTF12hsx	–	–	4.974 ± 0.131	–	4.974 ± 0.131
2013K	–	4.770 ± 0.103	4.721 ± 0.090	4.831 ± 0.093	4.721 ± 0.090
2013ab	–	–	4.777 ± 0.081	4.708 ± 0.082	4.777 ± 0.081
2013am†	–	4.468 ± 0.079	4.670 ± 0.105	4.533 ± 0.105	4.468 ± 0.079
2013bu	–	–	4.573 ± 0.081	4.685 ± 0.079	4.685 ± 0.079
2013by	–	4.874 ± 0.087	4.762 ± 0.101	4.995 ± 0.121	4.874 ± 0.087
2013ej	4.722 ± 0.091	4.736 ± 0.058	4.742 ± 0.073	4.888 ± 0.070	4.732 ± 0.049
2013fs	–	–	4.857 ± 0.085	4.837 ± 0.079	4.837 ± 0.079
2013hj	–	–	4.973 ± 0.075	5.035 ± 0.074	5.035 ± 0.074
iPTF13dkz	–	–	4.932 ± 0.122	–	4.932 ± 0.122
LSQ13dpa	–	–	4.968 ± 0.095	4.943 ± 0.128	4.968 ± 0.095
2014G	–	4.699 ± 0.076	4.946 ± 0.076	4.949 ± 0.077	4.699 ± 0.076
2014cx	–	4.914 ± 0.068	4.893 ± 0.084	4.820 ± 0.087	4.914 ± 0.068
2014cy	–	–	4.607 ± 0.088	4.560 ± 0.088	4.560 ± 0.088
ASASSN-14dq	–	–	4.864 ± 0.083	4.892 ± 0.085	4.864 ± 0.083
2014dw	–	–	4.746 ± 0.103	4.717 ± 0.131	4.746 ± 0.103
ASASSN-14ha†	–	4.433 ± 0.078	4.502 ± 0.089	4.651 ± 0.107	4.433 ± 0.078
OGLE14-18	–	–	4.835 ± 0.090	–	4.835 ± 0.090
2015V	–	–	4.696 ± 0.085	4.600 ± 0.091	4.696 ± 0.085
2015W	–	–	4.832 ± 0.086	4.931 ± 0.096	4.832 ± 0.086
2015an	–	–	4.730 ± 0.087	4.944 ± 0.106	4.730 ± 0.087
2015ba	–	4.442 ± 0.074	4.597 ± 0.087	4.905 ± 0.080	4.442 ± 0.074
2015bs	–	5.063 ± 0.077	4.941 ± 0.089	4.897 ± 0.098	5.063 ± 0.077
2015cz	–	–	4.846 ± 0.081	4.938 ± 0.089	4.846 ± 0.081
ASASSN-15oz	–	4.877 ± 0.071	5.082 ± 0.091	5.064 ± 0.097	4.877 ± 0.071
2016X	–	–	4.844 ± 0.099	4.865 ± 0.107	4.844 ± 0.099
2016aq†	–	4.625 ± 0.076	4.683 ± 0.095	4.666 ± 0.112	4.625 ± 0.076
2016bkv†	–	–	4.609 ± 0.085	4.309 ± 0.094	4.609 ± 0.085
2016gfy	–	4.827 ± 0.068	4.958 ± 0.084	4.935 ± 0.087	4.827 ± 0.068
2016ija	–	–	4.727 ± 0.098	4.826 ± 0.132	4.727 ± 0.098
2017it	–	–	4.890 ± 0.073	4.856 ± 0.070	4.856 ± 0.070
2017ahn	–	–	4.860 ± 0.094	4.840 ± 0.126	4.860 ± 0.094
2017eaw	4.970 ± 0.056	4.933 ± 0.061	4.975 ± 0.075	4.964 ± 0.077	4.953 ± 0.041
2017gmr	–	–	5.091 ± 0.081	5.057 ± 0.082	5.091 ± 0.081
2018aoq†	4.541 ± 0.052	–	4.506 ± 0.072	4.567 ± 0.068	4.551 ± 0.041
2018cuf	–	4.859 ± 0.077	4.810 ± 0.090	4.876 ± 0.105	4.859 ± 0.077
2018hwm	–	4.361 ± 0.075	4.414 ± 0.091	4.430 ± 0.091	4.361 ± 0.075

Notes. L_{prog} values are in units of L_{\odot} , and quoted uncertainties are 1σ errors. Errors on $\log L_{\text{prog}}(L_{[\text{O I}]^{350\text{d}}})$, $\log L_{\text{prog}}(M_{\text{Ni}})$, $\log L_{\text{prog}}(M_V^{50\text{d}})$, and $\log L_{\text{prog}}$ are random and do not include the systematic calibration error of 0.043 dex.

†SNe in the VL sample with $M_R^{\text{max}} > -16.8$.

Table 8. Histograms for M_R^{max} .

M_R^{max} range	NC	CVL	1.83 CVL – NC	VL
–17.8, –18.8	16	8	–1	7
–16.8, –17.8	37	21	1	12
–15.8, –16.8	15	21	23	12
–14.8, –15.8	6	11	14	7

relation between $\log L_{\text{prog}}$ and $\log M_{\text{Ni}}$ confirms the finding of Fraser et al. (2011) and Kushnir (2015).

I use the procedure described in Section 3.4 to compute the parameters of the linear correlations mentioned above, obtaining

$$\log L_{\text{prog}} = 4.554(42) + 0.379(58) \log L_{[\text{O I}]^{350\text{d}}} \quad (14)$$

(L_{prog} in L_{\odot} and $L_{[\text{O I}]^{350\text{d}}}$ in $10^{38} \text{ erg s}^{-1}$) with $\sigma_0 = 0.053$ and $\hat{\sigma} = 0.143$, valid in the range $-0.54 \leq \log L_{[\text{O I}]^{350\text{d}}} \leq 1.09$,

$$\log L_{\text{prog}} = 5.521(147) + 0.502(87) \log M_{\text{Ni}} \quad (15)$$

12, and 10, respectively, is of 0.1 per cent. The resulting cor-

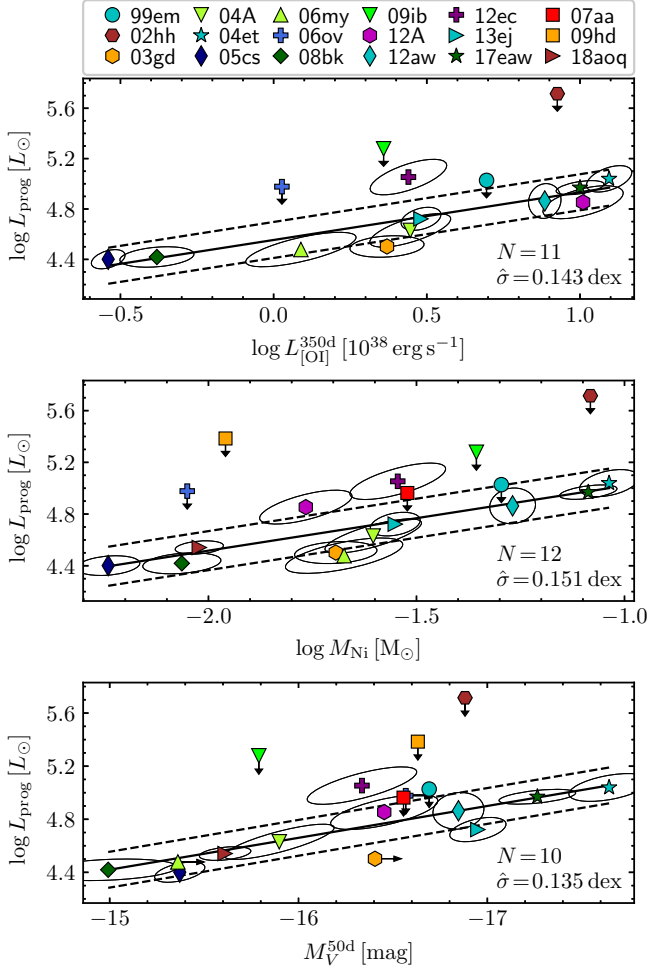


Figure 4. Progenitor luminosity against $L_{[\text{O I}]}^{350\text{d}}$ (top panel), ^{56}Ni mass (middle panel), and $M_V^{50\text{d}}$ (bottom panel). Solid lines are straight line fits and dashed lines are $\pm 1 \hat{\sigma}$ limits. Ellipses are 1σ confidence regions, while arrows indicate upper limits.

(M_{Ni} in M_{\odot}) with $\sigma_0 = 0.066$ and $\hat{\sigma} = 0.151$, valid in the range $-2.24 \leq \log M_{\text{Ni}} \leq -1.04$, and

$$\log L_{\text{prog}} = 0.820(692) - 0.240(42)M_V^{50\text{d}} \quad (16)$$

with $\sigma_0 = 0.060$ and $\hat{\sigma} = 0.135$, valid in the range $-17.7 \leq M_V^{50\text{d}} \leq -15.0$. In these expressions, numbers in parentheses are 1σ errors in units of 0.001.

I also compute the linear dependence of $\log L_{\text{prog}}$ on two SN II observables, obtaining

$$\log L_{\text{prog}} = 4.835 + 0.281 \log L_{[\text{O I}]}^{350\text{d}} + 0.151 \log M_{\text{Ni}} \quad (17)$$

with $\sigma_0 = 0.057$ dex and $\hat{\sigma} = 0.147$ dex,

$$\log L_{\text{prog}} = 4.148 + 0.348 \log M_{\text{Ni}} - 0.070M_V^{50\text{d}} \quad (18)$$

with $\sigma_0 = 0.006$ dex and $\hat{\sigma} = 0.138$ dex, and

$$\log L_{\text{prog}} = 3.758 - 0.053M_V^{50\text{d}} + 0.294 \log L_{[\text{O I}]}^{350\text{d}} \quad (19)$$

with $\sigma_0 = 0.004$ dex and $\hat{\sigma} = 0.139$ dex. Those correlations are shown in Fig. 5. The $\hat{\sigma}$ values do not decrease by adding a third variable to the correlation, which means that the inclusion of that variable does not provide further information about L_{prog} . This is probably because $M_V^{50\text{d}}$ is correlated with

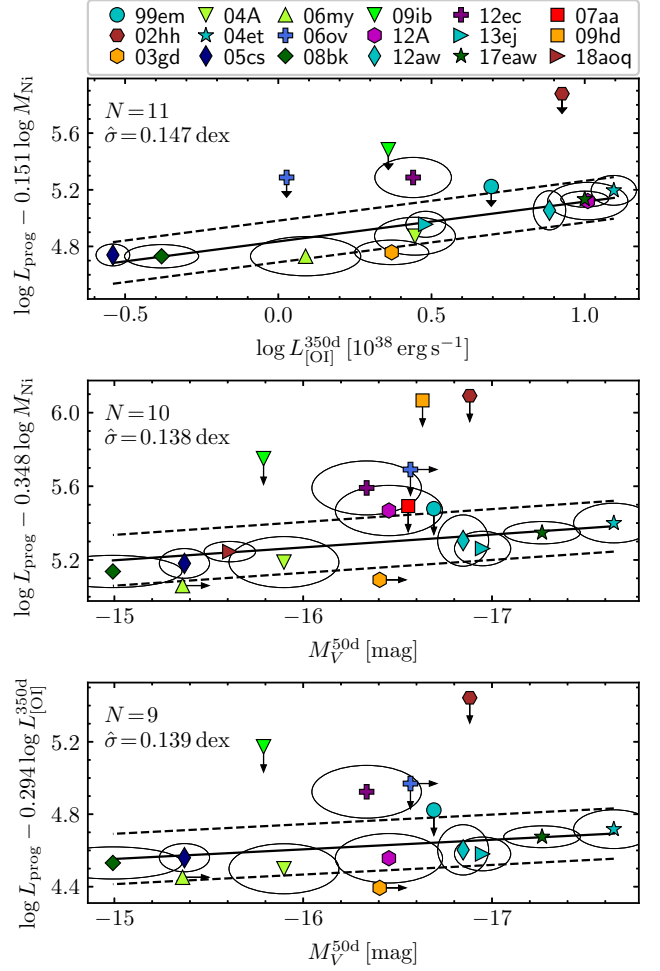


Figure 5. Progenitor luminosity against M_{Ni} and $L_{[\text{O I}]}^{350\text{d}}$ (top panel), M_{Ni} and $M_V^{50\text{d}}$ (middle panel), and $L_{[\text{O I}]}^{350\text{d}}$ and $M_V^{50\text{d}}$ (bottom panel). Lines, ellipses, and arrows have the same meaning as in Fig. 4.

M_{Ni} (e.g. Hamuy 2003; Spiro et al. 2014; Valenti et al. 2016; Rodríguez et al. 2021), while the luminosity of the [O I] doublet depends not only on oxygen mass but also on M_{Ni} (e.g. Elmhamdi et al. 2003).

4.1.2 Progenitor luminosity estimates

Equations (14), (15), and (16) allow us to compute $\log L_{\text{prog}}$ from $\log L_{[\text{O I}]}^{350\text{d}}$, $\log M_{\text{Ni}}$, and $M_V^{50\text{d}}$, respectively. The random error on the measured $\log L_{\text{prog}}$ is given by

$$\sigma_{\log L_{\text{prog}}} = \sqrt{(\partial \log L_{\text{prog}} / \partial x)^2 \sigma_x^2 + \sigma_0^2}, \quad (20)$$

where $x = \log L_{[\text{O I}]}^{350\text{d}}$, $\log M_{\text{Ni}}$, or $M_V^{50\text{d}}$, while the systematic uncertainty on $\log L_{\text{prog}}$ due to the calibration error is of $\hat{\sigma} / \sqrt{N} = 0.043$ dex.

I compute $\log L_{\text{prog}}$ for the 44 SNe with $\log L_{[\text{O I}]}^{350\text{d}}$ measurements ($\log L_{\text{prog}}(L_{[\text{O I}]}^{350\text{d}})$), the 111 SNe with $\log M_{\text{Ni}}$ estimates ($\log L_{\text{prog}}(M_{\text{Ni}})$), and the 93 SNe with $M_V^{50\text{d}}$ values ($\log L_{\text{prog}}(M_V^{50\text{d}})$). Those estimates are listed in Columns 3, 4, and 5 of Table 7, respectively. Of the reported $\log L_{\text{prog}}$ values, 14 are computed by extrapolating equations (14)–(16).

Table 9. Statistics of the $\log(L_{\text{prog}}/L_{\odot})$ distributions.

Sample	N	Mean	$\hat{\sigma}$	Min	Max
SBC	150	4.716	0.18	4.361(75)	5.091(81)
$L_{\text{prog}}(\text{phot})$	12	4.706	0.24	4.401(76)	5.053(141)
$L_{\text{prog}}(M_{\text{Ni}})$	111	4.757	0.18	4.375(85)	5.125(111)
$L_{\text{prog}}(L_{[\text{O I}] }^{350\text{d}})$	44	4.719	0.20	4.349(57)	5.063(77)
$L_{\text{prog}}(M_V^{50\text{d}})$	92	4.771	0.18	4.309(94)	5.073(95)

Note: Numbers in parentheses are 1σ random errors in units of 0.001.

Specifically, SNe 1992H, 1996W, 2007it, and 2015bs have $\log L_{[\text{O I}] }^{350\text{d}} > 1.09$ dex; SNe 1992H, 1996W, 2007it, 2009ay, ASASSN-15oz, and 2017gmr have $\log M_{\text{Ni}} > -1.04$ dex; and SNe 1994N, 2003B, 2003Z, and 2016bkv have $M_V^{50\text{d}} > -15$ mag. For these SNe, the mean offsets of their extrapolated $\log L_{\text{prog}}(L_{[\text{O I}] }^{350\text{d}})$, $\log L_{\text{prog}}(M_{\text{Ni}})$, and $\log L_{\text{prog}}(M_V^{50\text{d}})$ values with respect to the $\log L_{\text{prog}}$ estimates computed with parameters lying within the validity ranges are of 0.03 ± 0.07 , 0.03 ± 0.03 , and 0.10 ± 0.14 dex, respectively. This indicates that the extrapolation of equations (14)–(16) for the SNe mentioned above provides appropriate $\log L_{\text{prog}}$ values.

The mean errors on $\log L_{\text{prog}}(L_{[\text{O I}] }^{350\text{d}})$, $\log L_{\text{prog}}(M_{\text{Ni}})$, and $\log L_{\text{prog}}(M_V^{50\text{d}})$ are of 0.086, 0.101, and 0.105 dex, respectively, corresponding to L_{prog} errors of 20, 23, and 24 per cent, respectively. The calibration error and σ_0 induce 67, 64, and 55 per cent of the total error on $\log L_{\text{prog}}(L_{[\text{O I}] }^{350\text{d}})$, $\log L_{\text{prog}}(M_{\text{Ni}})$, and $\log L_{\text{prog}}(M_V^{50\text{d}})$, respectively.

Fig. 6 shows the differences between $\log L_{\text{prog}}(M_{\text{Ni}})$ and $\log L_{\text{prog}}(L_{[\text{O I}] }^{350\text{d}})$ (top panel), $\log L_{\text{prog}}(M_V^{50\text{d}})$ and $\log L_{\text{prog}}(M_{\text{Ni}})$ (middle panel), and $\log L_{\text{prog}}(L_{[\text{O I}] }^{350\text{d}})$ and $\log L_{\text{prog}}(M_V^{50\text{d}})$ (bottom panel). For those differences I compute mean offsets of 0.026, 0.017, and -0.032 dex, respectively, and $\hat{\sigma}$ values of 0.102, 0.110, and 0.128 dex, respectively. These offsets are consistent with zero within $1.7 \hat{\sigma}/\sqrt{N}$, meaning that the $\log L_{\text{prog}}$ values computed from $\log L_{[\text{O I}] }^{350\text{d}}$, $\log M_{\text{Ni}}$, and $M_V^{50\text{d}}$ are statistically consistent. Therefore, I adopt the $\log L_{\text{prog}}$ value with the lowest uncertainty as the best $\log L_{\text{prog}}$ estimate. If $\log L_{\text{prog}}(\text{phot})$ is available, then I adopt the weighted average between this value and the $\log L_{\text{prog}}$ estimate with the lowest error as the best $\log L_{\text{prog}}$ value. These estimates are listed in Column 6 of Table 7.

4.2 Progenitor luminosity distribution

Fig. 7 shows the progenitor luminosity distribution for the SBC sample, along with the distributions for the $\log L_{\text{prog}}(\text{phot})$, $\log L_{\text{prog}}(M_{\text{Ni}})$, $\log L_{\text{prog}}(L_{[\text{O I}] }^{350\text{d}})$, and $\log L_{\text{prog}}(M_V^{50\text{d}})$ values. The mean, $\hat{\sigma}$, minimum, and maximum values of these distributions are summarized in Table 9. The minimum and maximum values of the distributions for $\log L_{\text{prog}}(M_{\text{Ni}})$, $\log L_{\text{prog}}(L_{[\text{O I}] }^{350\text{d}})$, and $\log L_{\text{prog}}(M_V^{50\text{d}})$ are statistically consistent with those of the $\log L_{\text{prog}}(\text{phot})$ distribution. In other words, the SNe in this work with the lowest (largest) ^{56}Ni mass, the lowest (highest) $\log L_{[\text{O I}] }^{350\text{d}}$ estimate, and the highest (lowest) $M_V^{50\text{d}}$ value have progenitor luminosities consistent with the luminosity of the faintest (brightest) progenitor detected in pre-explosion images. The apparent upper limit of $\log(L/L_{\odot}) \approx 5.1$ for the progenitor luminosity is consistent with that found by Smartt (2015).

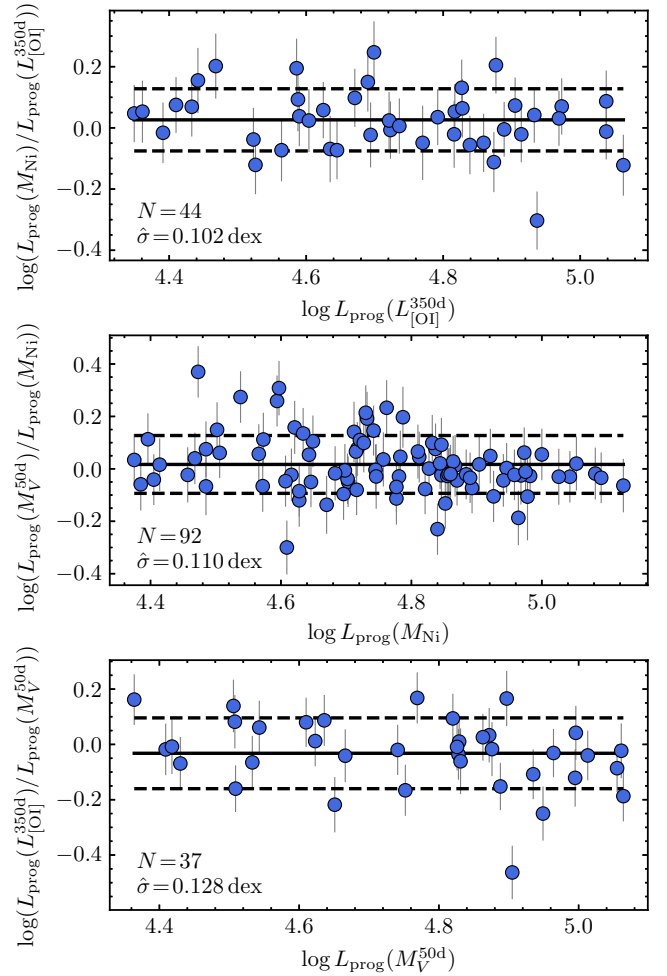


Figure 6. Differences between $\log L_{\text{prog}}$ values computed with M_{Ni} and $L_{[\text{O I}] }^{350\text{d}}$ (top panel), $M_V^{50\text{d}}$ and M_{Ni} (middle panel), and $L_{[\text{O I}] }^{350\text{d}}$ and $M_V^{50\text{d}}$ (bottom panel). Solid lines indicate mean values, while dashed lines are the $\pm 1 \hat{\sigma}$ limits around the means. Error bars are 1σ errors.

4.3 Comparison with RSG luminosities

For the comparison between luminosities of SN II progenitors in the SBC sample and of RSGs in the samples of LMC, SMC, M31 and M33, I select RSGs with $\log(L/L_{\odot}) \geq 4.361$, corresponding to the minimum $\log(L/L_{\odot})$ value in the SBC sample.

4.3.1 Luminosity distributions

The top panel of Fig. 8 shows the distribution for the progenitor luminosities in the SBC sample and the luminosity distributions for the RSGs in LMC, SMC, M31, and M33. We see a conspicuous absence of SN II progenitors with $\log(L/L_{\odot}) > 5.1$ with respect to the RSG samples, which will be analysed in Section 4.3.2. We also see that for $\log(L/L_{\odot}) < 4.6$ the SBC sample has a lower number density than the RSGs sets. The latter is most likely due to the SBC sample is not complete for low luminosity SNe II. Indeed, using equation (16), progenitors with $\log(L_{\text{prog}}/L_{\odot}) < 4.6$ correspond to SNe II with $M_V^{50\text{d}} > -15.8$, which characterizes the population of low luminosity SNe II (see e.g. Fig. 11 of

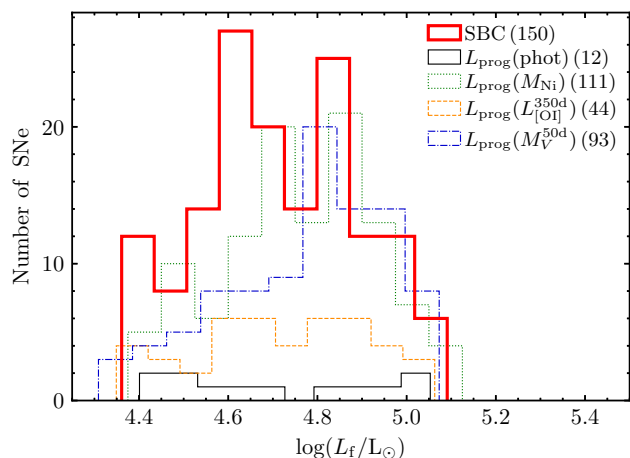


Figure 7. Histogram for the final luminosities in the selection-bias corrected sample (red thick line), along with the histograms for the $\log L_{\text{prog}}$ values computed with progenitor photometry (black thin line), M_{Ni} (green dotted line), $L_{\text{[O I]}}^{350\text{d}}$ (orange dashed line), and $M_V^{50\text{d}}$ (blue dash-dotted line). Numbers in parentheses are the sample sizes.

Yang et al. 2021). In order to avoid the low completeness of low luminosity SNe II, I select from the SBC sample those SNe with $\log(L_{\text{prog}}/L_{\odot}) \geq 4.6$, which I refer to as the gold sample. Given the high completeness of the SNe that are not low luminosity SNe II (see Section 3.3), I consider the gold sample to be complete to $\log(L/L_{\odot}) = 4.6$ dex.

The bottom panel of Fig. 8 shows the cumulative luminosity distributions for the gold sample and the RSGs in LMC, SMC, M31, and M33 in the luminosity domain of the gold sample ($4.6 \leq \log(L/L_{\odot}) \leq 5.091$). Using the k -sample AD test to compare the gold sample with these RSG sets, I obtain T_{AD} (p -value) of 0.22 (0.28), -0.39 (0.55), -0.52 (0.64), and -0.29 (0.50), respectively. Therefore, the null hypothesis that the SN II progenitors in the gold sample and RSGs with $4.6 \leq \log(L/L_{\odot}) \leq 5.091$ are drawn from a common luminosity distribution cannot be rejected at a significance level of at least 28 per cent. This result supports RSGs as SN II progenitors.

4.3.2 The RSG problem

Fig. 9 shows the cumulative luminosity distributions for the gold sample and RSGs in LMC, SMC, M31, and M33 with $\log(L/L_{\odot}) \geq 4.6$. As previously mentioned, there is a conspicuous absence of SN II progenitors with $\log(L/L_{\odot}) > 5.1$ with respect to the RSG samples. For those samples, between 13 and 18 per cent of the RSGs with $\log(L/L_{\odot}) \geq 4.6$ have $\log(L/L_{\odot}) > 5.1$. If such RSGs explode as SNe II, then the gold sample should have between 16 and 25 progenitors with $\log(L/L_{\odot}) > 5.1$. The Poissonian probability of not observing such events is given by

$$P = \frac{e^{-n_{\text{exp}}} n_{\text{exp}}^{n_{\text{obs}}}}{n_{\text{obs}}!}, \quad (21)$$

where n_{exp} and n_{obs} are the expected and observed number of progenitors with $\log(L/L_{\odot}) > 5.1$, respectively. For $n_{\text{obs}} = 0$ and $n_{\text{exp}} = 16$ (25), $P = 1.1 \times 10^{-7}$ (1.4×10^{-11}), corresponding to a significance of 5.3σ (6.8σ). Since the calculation does

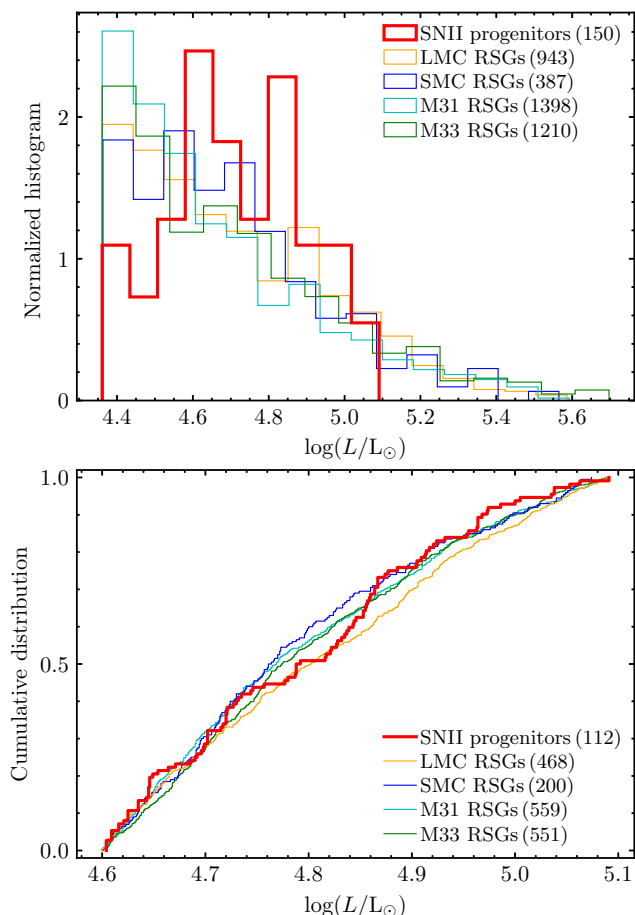


Figure 8. Top panel: histograms for the progenitor luminosities in the SBC sample (thick red line) and the luminosities of the RSGs in LMC, SMC, M31, and M33 with $\log(L/L_{\odot}) \geq 4.361$ (thin lines). Bottom panel: cumulative distributions for the progenitor luminosities in the gold sample (thick red line) and the luminosities in the RSG samples in the luminosity domain of the gold sample (thin lines). Numbers in parentheses are the sample sizes.

not include luminosity uncertainties, the inferred significance values for the RSG problem are overestimated. To include the effect of luminosity errors, I perform 10^4 simulations varying randomly luminosities in the SBC and RSG samples according to their statistical errors (assumed normal). For each realization, I construct a gold sample by selecting the $\log(L/L_{\odot})$ values greater than 4.6 dex from the simulated SBC sample. The $\log(L/L_{\odot})$ estimates in the simulated gold sample are then shifted by a constant, which is randomly selected from a normal distribution with zero mean and standard deviation equal to the systematic calibration error. For each of the four simulated RSG samples, I compute the ratio between the number of RSGs with $\log(L/L_{\odot}) > 5.1$ and with $\log(L/L_{\odot})$ greater than the minimum $\log(L/L_{\odot})$ value in the simulated gold sample. Then, I compute n_{exp} and n_{obs} and, using equation (21), P and the corresponding significance.

Fig. 10 shows the histograms for the significance values of the RSG problem computed with simulated gold and RSG samples. For the comparison between the gold sample and the LMC, SMC, M31, and M33 sets, the mean significance values (in σ units) are of $4.8^{+1.0}_{-1.3}$, $4.3^{+1.0}_{-1.3}$, $5.2^{+1.0}_{-1.1}$, and $5.8^{+1.0}_{-1.1}$ (95 per cent confidence interval), respectively. Combining the

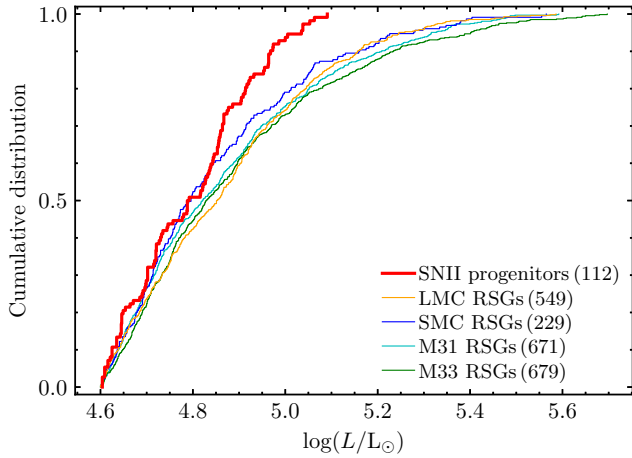


Figure 9. Cumulative distributions for the progenitor luminosities in the gold sample (red thick line) and the luminosities of the RSGs in LMC, SMC, M31, and M33 with $\log(L/L_{\odot}) \geq 4.6$ (thin lines). Numbers in parentheses are the sample sizes.

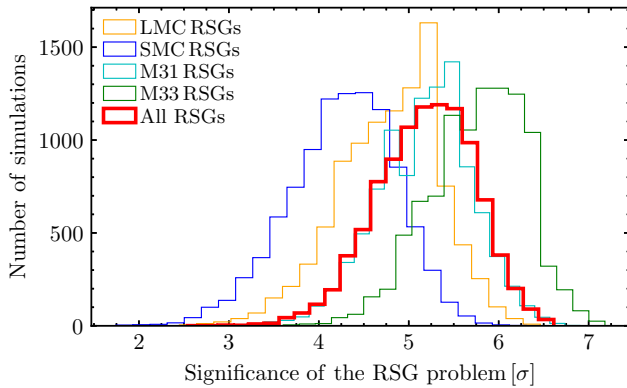


Figure 10. Histograms for the significance values of the RSG problem computed with 10^4 simulations of the gold sample, the four RSG samples (thin lines), and the combined RSG sample (thick red line).

four RSG samples into a single data set and performing the simulation described earlier, I obtain a mean significance of $5.2 \pm 0.5 \sigma$ ($1 \hat{\sigma}$ error). Therefore, the RSG problem is statistically significant.

5 DISCUSSION

5.1 Comparison with initial masses from models

I now compare the progenitor luminosities calculated in this work with initial masses reported in the literature computed with models. For this comparison, progenitor luminosities have to be transformed to initial masses using an initial mass-final luminosity relation (MLR). This relation depends on the stellar evolution model adopted in each work.

Morozova et al. (2018) and Martínez et al. (2020, 2022) reported M_i values inferred by fitting hydrodynamical models to SN data. Morozova et al. (2018) used multi-band light-curve models generated with the SNEC code (Morozova et al. 2015), while Martínez et al. (2020, 2022) used bolometric light curves and expansion velocity curves

Table 10. SNe with initial masses estimated with SUMO models.

SN	μ	E_{B-V}^{host}	M_i/M_{\odot}	Reference [†]
1997D	30.64	0.0	9	a
1999em	30.34	0.06	13 ± 1	b
2004A	31.35	0.0	12	c
2004et	28.70	0.117	15	d
2008bk	27.84	0.0	9	a
2012A	29.96	0.009	15	e
2012aw	29.98	0.046	15	f
2012ec	31.19	0.087	13–15	g
2013ej	29.93	0.0	12–15	h
2014G	31.94	0.20	15–19	i
2014cx	31.74	0.0	15	j
ASASSN-14dq	33.26	0.0	15	j
2015W	33.74	0.0	15	j
2015bs	35.40	0.0	15–25	k
ASASSN-15oz	32.30	0.0	15–19	l
2016aqf	30.16	0.0	12 ± 3	m
2016gfy	32.36	0.14	15	n
2017eaw	29.44	0.0	15	o
2018cuf	33.11	0.11	12–15	p

[†](a): Jerkstrand et al. (2018); (b): Davies & Beasor (2018); (c): Silverman et al. (2017); (d): Jerkstrand et al. (2012); (e): Tomasella et al. (2013); (f): Jerkstrand et al. (2014); (g): Jerkstrand et al. (2015); (h): Yuan et al. (2016); (i): Terreran et al. (2016); (j): Valenti et al. (2016); (k): Anderson et al. (2018); (l): Bostroem et al. (2019); (m): Müller-Bravo et al. (2020); (n): Singh et al. (2019); (o): Van Dyk et al. (2019); (p): Dong et al. (2020).

calculated with the model of Bersten et al. (2011). In addition, 19 SNe used in the present study have M_i estimates computed by comparing late-time spectra with spectral models generated with the SUMO code (Jerkstrand et al. 2011, 2012). These SNe, along with the reported μ , E_{B-V}^{host} , and M_i values are collected in Table 10. Morozova et al. (2018), Martínez et al. (2020, 2022), and the SUMO code adopted non-rotating RSGs models with solar composition and M_i between 9 and $25 M_{\odot}$ as progenitors. Specifically, Morozova et al. (2018) and the SUMO code used RSG models computed with the KEPLER code (e.g. Woosley et al. 2002), while Martínez et al. (2020, 2022) computed RSG models using the MESA code (e.g. Farmer et al. 2016). Using initial masses and final luminosities for $M_i \leq 25 M_{\odot}$ reported in Woosley et al. (2002) and Farmer et al. (2016) (for non-rotating models), I derive MLRs for KEPLER and MESA codes, given by $\log(M_i/M_{\odot}) = -1.263 + 0.495 \log(L_{\text{prog}}/L_{\odot})$ and $\log(M_i/M_{\odot}) = -1.235 + 0.491 \log(L_{\text{prog}}/L_{\odot})$, respectively.

To compare the initial masses calculated with the three models mentioned above (SNEC, the Bersten’s model, and SUMO) with the $\log L_{\text{prog}}$ values computed from $L_{[\text{O I}]}^{350d}$, M_{Ni} , or M_V^{50d} , I first recompute $\log L_{\text{prog}}$ using the distances and reddenings adopted in the respective work, and then convert $\log L_{\text{prog}}$ to $\log M_i$ ($\log M_i(L_{\text{prog}})$) using the corresponding MLR. In the case of Martínez et al. (2022), the authors do not provide E_{B-V}^{host} values. Instead, they report a variable called *scale*, equivalent to the intrinsic luminosity divided by the observed luminosity uncorrected for host galaxy extinction. The *scale* parameter accounts for host galaxy extinction and for the difference between the adopted distance and the true distance. Since I adopt the distances of Martínez et al. (2022), I assume that they correspond to the true values, so the host galaxy extinction affecting the bolo-

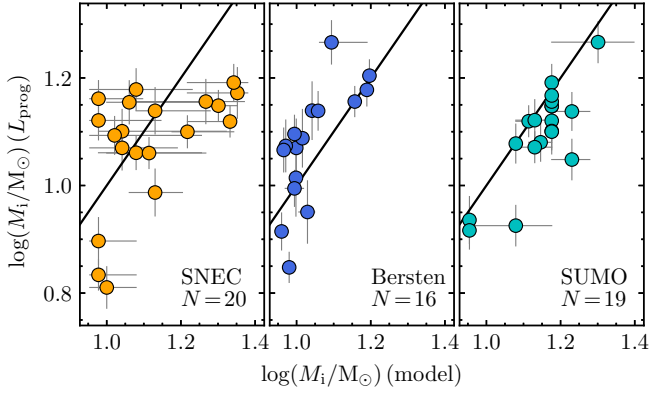


Figure 11. Initial masses estimated from the recalibrated $\log L_{\text{prog}}$ values against those computed by [Morozova et al. \(2018\)](#) using SNEC (left-hand panel), by [Martinez et al. \(2020, 2022\)](#) using the model of [Bersten et al. \(2011\)](#) (middle panel), and those computed with SUMO models (right-hand panel). Solid lines are one-to-one correspondences.

metric light curve is $A_{\text{bol}} = 2.5 \log(\text{scale})$. [Rodríguez et al. \(2021\)](#) computed $A_{\text{bol}}/E_{B-V} = 1.68$, so I adopt $E_{B-V}^{\text{host}} = 1.49 \log(\text{scale})$. Among the SNe in common between the sample of [Martinez et al. \(2022\)](#) and the one used in this work, SNe 2004ej and 2007od have *scale* values significantly lower than unity, which result in negative E_{B-V}^{host} values of -0.14 and -0.39 mag, respectively. The low *scale* values for these SNe could be due to, for example, an overestimation of their distances. Since the negative E_{B-V}^{host} values of SNe 2004ej and 2007od have no physical meaning, I do not include those SNe in the comparison with the model of [Bersten et al. \(2011\)](#).

Fig. 11 shows the $\log M_i(L_{\text{prog}})$ values against the initial masses of [Morozova et al. \(2018\)](#) (left-hand panel), [Martinez et al. \(2020, 2022\)](#) (middle panel), and those computed with the SUMO models (right-hand panel). For each comparison I fit a straight line, whose slope (b) is listed in Column 3 of Table 11, and a straight line with slope of unity, whose y -intercept (a) is listed in Column 4 of Table 11. To test if two methods of measurement are statistically consistent, it is necessary to test if b and a are statistically consistent with unity and zero, respectively. For this task I use the one-sample t -test, where the p -values for the null hypotheses $b = 1$ and $a = 0$ are listed in Columns 5 and 6 of Table 11, respectively. I choose a significance level of 0.05 to accept the null hypothesis for b and a . Based on this criterion, the initial masses computed with the models of [Bersten et al. \(2011\)](#) and SUMO are statistically consistent with $\log M_i(L_{\text{prog}})$. On the other hand, the b value for SNEC is significantly lower than unity, so the initial masses reported by [Morozova et al. \(2018\)](#) are not consistent with $\log M_i(L_{\text{prog}})$.

I also compare $\log M_i(L_{\text{prog}})$ with initial masses computed by [Maund \(2017\)](#) through the age-dating technique, and by other authors using three different hydrodynamical models: [Pumo et al. \(2017\)](#) based on the model of [Pumo & Zampieri \(2011\)](#) (PZ11), [Ricks & Dwarkadas \(2019\)](#) using the STELLA code ([Blinnikov et al. 1998](#)), and [Utrobin & Chugai \(2019\)](#) based on the CRAB code ([Utrobin 2004](#)). For these works, the MLR is not straightforward to obtain. For the sake of simplicity, I assume the average of the KEPLER and MESA MLRs, i.e., $\log(M_i/M_\odot) = -1.249 + 0.493 \log(L_{\text{prog}}/L_\odot)$.

Fig. 12 shows the comparisons between $\log M_i(L_{\text{prog}})$ and

Table 11. Slopes and y -intercepts of the $\log M_i$ comparisons.

Method	N	b	a	$p_{b=1}$	$p_{a=0}$
SNEC	20	0.43(17)	-0.043(34)	0.0	0.22
Bersten	16	0.98(27)	0.035(29)	0.94	0.25
SUMO	19	0.88(14)	-0.049(24)	0.41	0.06
PZ11	11	0.21(36)	-0.159(48)	0.06	0.01
CRAB	8	0.39(28)	-0.279(48)	0.07	0.0
STELLA	8	-0.50(17)	-0.045(68)	0.0	0.53
Age-dating	11	0.60(22)	-0.054(35)	0.10	0.16

Note: Numbers in parentheses are 1σ errors in units of the last significant digit.

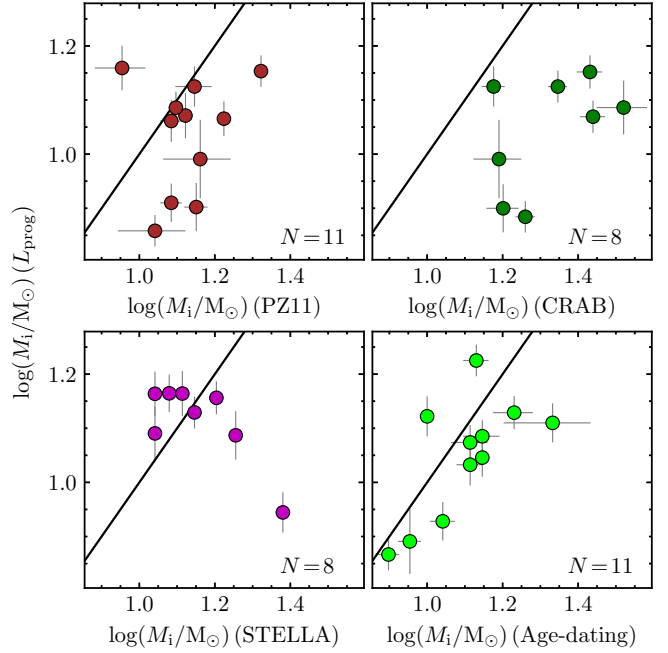


Figure 12. Initial masses estimated from the recalibrated $\log L_{\text{prog}}$ values against those used in [Pumo et al. \(2017\)](#) based on the model of [Pumo & Zampieri \(2011\)](#) (top left panel), in [Utrobin & Chugai \(2019\)](#) computed with CRAB (top right panel), those computed by [Ricks & Dwarkadas \(2019\)](#) using STELLA (bottom left panel), and by [Maund \(2017\)](#) using the age-dating method (bottom right panel). Solid lines are one-to-one correspondences.

initial masses calculated with each of the four methods mentioned above, while the corresponding b , a , and p -values are listed in Table 11. Of those methods, only the age-dating technique provides initial masses statistically consistent with $\log M_i(L_{\text{prog}})$. The negative b value for STELLA is incompatible with unity, while the a values for PZ11 and CRAB are significantly lower than zero, so the initial masses computed with these models are not consistent with $\log M_i(L_{\text{prog}})$. In particular, the M_i estimates computed with the model of PZ11 and the CRAB code are, on average, 1.4 and 1.9 times larger than those inferred from the recalibrated $\log L_{\text{prog}}$ values, respectively. The overestimation of the initial masses calculated with the CRAB code was previously reported by [Utrobin & Chugai \(2008, 2009\)](#).

5.2 Systematics

5.2.1 BCs for RSGs

The BC is an important source of uncertainty in determining $\log L_{\text{prog}}$ values. For eight of the twelve SN II progenitors used to compute the correlations between $\log L_{\text{prog}}$ and SN observables, the adopted BC estimates correspond to the weighted average of the BC values for late-type RSGs ($\langle \text{BC} \rangle$). These $\langle \text{BC} \rangle$ estimates are based on only four RSGs (see [Davies & Beasar 2018](#)) so their values are not statistically robust, which could affect the inferred significance of the RSG problem. Assuming the average BC error of 0.15 dex as the $\hat{\sigma}$ around $\langle \text{BC} \rangle$, the standard error of the mean is of $\sigma_{\langle \text{BC} \rangle} = 0.075$ dex. If the true $\langle \text{BC} \rangle$ value were $3\sigma_{\langle \text{BC} \rangle}$ greater than the current estimate, the significance of the RSG problem would be reduced to $4.4 \pm 0.7\sigma$. This significance is greater than 3σ at a confidence level of 98 per cent, so the RSG problem is still statistically significant.

5.2.2 Calibration sample

The correlations between $\log L_{\text{prog}}$ and SN observables presented in Section 4.1.1 are based on 10–12 progenitors, so the correlation parameters could be misestimated due to the small sample sizes. Based on the observed $\hat{\sigma}$ values of about 0.14–0.15 dex and the current sample sizes, the true standard deviation around the correlations shown in Fig. 4 (σ_{true}) can be as low as 0.1 dex or as large as 0.27 dex at a 95 per cent confidence level.¹⁰ If the σ_{true} value is around 0.25 dex, then it would be necessary to double the calibration sample size in order to have a systematic calibration error similar to the current one.

6 CONCLUSION

In this work I have computed empirical correlations between luminosity of SN II progenitors and three SN observables: $L_{[\text{O} \text{I}]}^{350\text{d}}$, M_{Ni} , and $M_V^{50\text{d}}$. For this, I have used twelve SNe II with L_{prog} measured from progenitor photometry. Using these empirical correlations, I have estimated final luminosities for a sample of 112 SNe II. I have corrected this sample for selection bias and, discarding low luminosity SNe II, defined a gold sample of 112 SNe complete at $\log(L/L_{\odot}) = 4.6$ dex.

The main conclusions are the following:

- (1) Linear correlations between $\log L_{\text{prog}}$ and $\log L_{[\text{O} \text{I}]}^{350\text{d}}$, $\log M_{\text{Ni}}$, or $M_V^{50\text{d}}$ are strong and statistically significant. These correlations allow estimating L_{prog} with a precision of 20, 23, and 24 per cent, respectively.
- (2) The luminosity distribution for the gold sample is statistically consistent with those for RSGs in SMC, LMC, M31, and M33 with $4.6 \leq \log(L/L_{\odot}) \leq 5.091$. This reinforces the fact that SN II progenitors correspond to RSGs.

¹⁰ This result is computed assuming that residuals of the correlation fits have a normal parent distribution with standard deviation σ_{true} , for which the quantity $(\hat{\sigma}/\sigma_{\text{true}})^2\nu$ has a chi-square distribution with ν degrees of freedom (e.g. [Lu 1960](#)).

(3) The conspicuous absence of SN II progenitors with $\log(L/L_{\odot}) > 5.1$ with respect to what is observed in RSG luminosity distributions is significant at a $5.2 \pm 0.5\sigma$ level. This indicates that the RSG problem is statistically significant.

(4) Initial progenitor masses calculated with the hydrodynamical model of [Bersten et al. \(2011\)](#), the nebular spectra models generated with the SUMO code, and with the age-dating technique are statistically consistent with those computed from empirical $\log L_{\text{prog}}$ values and the corresponding MLR.

ACKNOWLEDGEMENTS

I thank K. Maguire, R. Roy, F. Huang, R. Dastidar, Y. Dong, D. O’Neill, and D. Tsvetkov for sharing spectra with me. This paper is part of a project that has received funding from the European Research Council (ERC) under the European Union’s Seventh Framework Programme, Grant agreement No. 833031 (PI: Dan Maoz). This work has made use of the Weizmann Interactive Supernova Data Repository (<https://www.wiserep.org>). This research has made use of the Spanish Virtual Observatory (<https://svo.cab.inta-csic.es>) project funded by MCIN/AEI/10.13039/501100011033/ through grant PID2020-112949GB-I00. This work is based in part on observations collected at the European Organisation for Astronomical Research in the Southern Hemisphere, Chile as part of PESSTO, (the Public ESO Spectroscopic Survey for Transient Objects Survey) ESO program 188.D-3003, 191.D-0935, 197.D-1075.

DATA AVAILABILITY

The data underlying this article will be shared on reasonable request to the corresponding author.

REFERENCES

- Anderson J. P., et al., 2018, *Nature Astronomy*, **2**, 574
 Arcavi I., et al., 2017, *Nature*, **551**, 210
 Benetti S., Cappellaro E., Turatto M., della Valle M., Mazzali P. A., Gouiffes C., 1994, *A&A*, **285**, 147
 Benetti S., et al., 2001, *MNRAS*, **322**, 361
 Bersten M. C., Benvenuto O., Hamuy M., 2011, *ApJ*, **729**, 61
 Bessell M., Murphy S., 2012, *PASP*, **124**, 140
 Black C. S., Milisavljevic D., Margutti R., Fesen R. A., Patnaude D., Parker S., 2017, *ApJ*, **848**, 5
 Blanton E. L., Schmidt B. P., Kirshner R. P., Ford C. H., Chromey F. R., Herbst W., 1995, *AJ*, **110**, 2868
 Blinnikov S. I., Eastman R., Bartunov O. S., Popolitov V. A., Woosley S. E., 1998, *ApJ*, **496**, 454
 Bose S., et al., 2013, *MNRAS*, **433**, 1871
 Bose S., et al., 2018, *ApJ*, **862**, 107
 Bostroem K. A., et al., 2019, *MNRAS*, **485**, 5120
 Cappellaro E., Danziger I. J., della Valle M., Gouiffes C., Turatto M., 1995, *A&A*, **293**, 723
 Chevalier R. A., 1976, *ApJ*, **207**, 872
 Cleveland W. S., Grosse E., Shyu W. M., 1992, in Chambers J. M., Hastie T. J., eds., *Statistical models in S*. Chapman and Hall, London, Chapt. 8, pp 309–376
 Clocchiatti A., et al., 1996, *AJ*, **111**, 1286

- Crockett R. M., Smartt S. J., Pastorello A., Eldridge J. J., Stephens A. W., Maund J. R., Mattila S., 2011, *MNRAS*, **410**, 2767
- Dastidar R., et al., 2018, *MNRAS*, **479**, 2421
- Davies B., Beasor E. R., 2018, *MNRAS*, **474**, 2116
- Davies B., Beasor E. R., 2020, *MNRAS*, **493**, 468
- Dessart L., Hillier D. J., Sukhbold T., Woosley S. E., Janka H. T., 2021, *A&A*, **652**, A64
- Díaz-Rodríguez M., Murphy J. W., Williams B. F., Dalcanton J. J., Dolphin A. E., 2021, *MNRAS*, **506**, 781
- Dong Y., et al., 2020, *ApJ*, **906**, 56
- Dwarkadas V. V., 2014, *MNRAS*, **440**, 1917
- Eldridge J. J., Tout C. A., 2004, *MNRAS*, **353**, 87
- Eldridge J. J., Guo N. Y., Rodrigues N., Stanway E. R., Xiao L., 2019, *Publ. Astron. Soc. Australia*, **36**, e041
- Elias-Rosa N., et al., 2011, *ApJ*, **742**, 6
- Elmhamdi A., 2011, *Acta Astron.*, **61**, 179
- Elmhamdi A., et al., 2003, *MNRAS*, **338**, 939
- Falk S. W., Arnett W. D., 1977, *ApJS*, **33**, 515
- Faran T., et al., 2014, *MNRAS*, **442**, 844
- Farmer R., Fields C. E., Petermann I., Dessart L., Cantiello M., Paxton B., Timmes F. X., 2016, *ApJS*, **227**, 22
- Filippenko A. V., 1997, *ARA&A*, **35**, 309
- Fitzpatrick E. L., 1999, *PASP*, **111**, 63
- Foreman-Mackey D., Hogg D. W., Lang D., Goodman J., 2013, *PASP*, **125**, 306
- Förster F., et al., 2018, *Nature Astronomy*, **2**, 808
- Fraser M., 2016, *MNRAS*, **456**, L16
- Fraser M., et al., 2011, *MNRAS*, **417**, 1417
- Fraser M., et al., 2014, *MNRAS*, **439**, L56
- Gómez G., López R., 2000, *AJ*, **120**, 367
- Graczyk D., et al., 2020, *ApJ*, **904**, 13
- Grassberg E. K., Imshennik V. S., Nadyozhin D. K., 1971, *Ap&SS*, **10**, 28
- Gutiérrez C. P., et al., 2017, *ApJ*, **850**, 89
- Hamuy M., 2003, *ApJ*, **582**, 905
- Hamuy M., Suntzeff N. B., Gonzalez R., Martin G., 1988, *AJ*, **95**, 63
- Huang F., et al., 2016, *ApJ*, **832**, 139
- Inserra C., et al., 2013, *A&A*, **555**, A142
- Jerkstrand A., Fransson C., Kozma C., 2011, *A&A*, **530**, A45
- Jerkstrand A., Fransson C., Maguire K., Smartt S., Ergon M., Spyromilio J., 2012, *A&A*, **546**, A28
- Jerkstrand A., Smartt S. J., Fraser M., Fransson C., Sollerman J., Taddia F., Kotak R., 2014, *MNRAS*, **439**, 3694
- Jerkstrand A., et al., 2015, *MNRAS*, **448**, 2482
- Jerkstrand A., Ertl T., Janka H. T., Müller E., Sukhbold T., Woosley S. E., 2018, *MNRAS*, **475**, 277
- Kushnir D., 2015, arXiv e-prints, p. arXiv:1506.02655
- Leonard D. C., et al., 2002, *PASP*, **114**, 35
- Leonard D. C., et al., 2006, *Nature*, **440**, 505
- Li S., Riess A. G., Busch M. P., Casertano S., Macri L. M., Yuan W., 2021, *ApJ*, **920**, 84
- Limongi M., Chieffi A., 2018, *ApJS*, **237**, 13
- Lu J. Y., 1960, *Journal of Farm Economics*, **42**, 910
- Maguire K., et al., 2010, *MNRAS*, **404**, 981
- Maguire K., et al., 2012, *MNRAS*, **420**, 3451
- Maíz-Apellániz J., Bond H. E., Siegel M. H., Lipkin Y., Maoz D., Ofek E. O., Poznanski D., 2004, *ApJ*, **615**, L113
- Martinez L., Bersten M. C., 2019, *A&A*, **629**, A124
- Martinez L., Bersten M. C., Anderson J. P., González-Gaitán S., Förster F., Folatelli G., 2020, *A&A*, **642**, A143
- Martinez L., et al., 2022, *A&A*, **660**, A41
- Massey P., Neugent K. F., Levesque E. M., Drout M. R., Courteau S., 2021a, *AJ*, **161**, 79
- Massey P., Neugent K. F., Dorn-Wallenstein T. Z., Eldridge J. J., Stanway E. R., Levesque E. M., 2021b, *ApJ*, **922**, 177
- Mattila S., Meikle W. P. S., Greimel R., 2004, *New Astron. Rev.*, **48**, 595
- Maund J. R., 2017, *MNRAS*, **469**, 2202
- Maund J. R., Smartt S. J., 2009, *Science*, **324**, 486
- Maund J. R., et al., 2013, *MNRAS*, **431**, L102
- Maund J. R., Reilly E., Mattila S., 2014a, *MNRAS*, **438**, 938
- Maund J. R., Mattila S., Ramirez-Ruiz E., Eldridge J. J., 2014b, *MNRAS*, **438**, 1577
- Maund J. R., Fraser M., Reilly E., Ergon M., Mattila S., 2015, *MNRAS*, **447**, 3207
- Meynet G., et al., 2015, *A&A*, **575**, A60
- Minkowski R., 1941, *PASP*, **53**, 224
- Morozova V., Piro A. L., Renzo M., Ott C. D., Clausen D., Couch S. M., Ellis J., Roberts L. F., 2015, *ApJ*, **814**, 63
- Morozova V., Piro A. L., Valenti S., 2018, *ApJ*, **858**, 15
- Müller-Bravo T. E., et al., 2020, *MNRAS*, **497**, 361
- Murphy J. W., Jennings Z. G., Williams B., Dalcanton J. J., Dolphin A. E., 2011, *ApJ*, **742**, L4
- Nazarov S. V., Okhmat D. N., Sokolovsky K. V., Denisenko D. V., 2018, *The Astronomer's Telegram*, **11498**, 1
- Neugent K. F., Levesque E. M., Massey P., Morrell N. I., Drout M. R., 2020, *ApJ*, **900**, 118
- O'Neill D., et al., 2019, *A&A*, **622**, L1
- O'Neill D., Kotak R., Fraser M., Mattila S., Pietrzyński G., Prieto J. L., 2021, *A&A*, **645**, L7
- Olivares E. F., et al., 2010, *ApJ*, **715**, 833
- Otsuka M., et al., 2012, *ApJ*, **744**, 26
- Pastorello A., et al., 2004, *MNRAS*, **347**, 74
- Pastorello A., et al., 2009a, *MNRAS*, **394**, 2266
- Pastorello A., et al., 2009b, *A&A*, **500**, 1013
- Pietrzyński G., et al., 2019, *Nature*, **567**, 200
- Poznanski D., 2013, *MNRAS*, **436**, 3224
- Pumo M. L., Zampieri L., 2011, *ApJ*, **741**, 41
- Pumo M. L., Zampieri L., Spiro S., Pastorello A., Benetti S., Cappellaro E., Manicò G., Turatto M., 2017, *MNRAS*, **464**, 3013
- Reguitti A., et al., 2021, *MNRAS*, **501**, 1059
- Ricks W., Dwarkadas V. V., 2019, *ApJ*, **880**, 59
- Riess A. G., Casertano S., Yuan W., Macri L. M., Scolnic D., 2019, *ApJ*, **876**, 85
- Rodrigo C., Solano E., 2020, in XIV.0 Scientific Meeting (virtual) of the Spanish Astronomical Society. p. 182
- Rodrigo C., Solano E., Bayo A., 2012, SVO Filter Profile Service Version 1.0, IVOA Working Draft 15 October 2012
- Rodríguez Ó., Clocchiatti A., Hamuy M., 2014, *AJ*, **148**, 107
- Rodríguez Ó., et al., 2019, *MNRAS*, **483**, 5459
- Rodríguez Ó., et al., 2020, *MNRAS*, **494**, 5882
- Rodríguez Ó., Meza N., Pineda-García J., Ramirez M., 2021, *MNRAS*, **505**, 1742
- Roy R., et al., 2011, *MNRAS*, **414**, 167
- Sahu D. K., Anupama G. C., Sridivya S., Muneer S., 2006, *MNRAS*, **372**, 1315
- Schlafly E. F., Finkbeiner D. P., 2011, *ApJ*, **737**, 103
- Schlegel E. M., 1990, *MNRAS*, **244**, 269
- Schmidt B. P., et al., 1993, *AJ*, **105**, 2236
- Scholz F. W., Stephens M. A., 1987, *Journal of the American Statistical Association*, **82**, 918
- Schwarz G., 1978, *Annals of Statistics*, **6**, 461
- Shivvers I., et al., 2017, *PASP*, **129**, 054201
- Silverman J. M., et al., 2012, *MNRAS*, **425**, 1789
- Silverman J. M., et al., 2017, *MNRAS*, **467**, 369
- Singh A., Kumar B., Moriya T. J., Anupama G. C., Sahu D. K., Brown P. J., Andrews J. E., Smith N., 2019, *ApJ*, **882**, 68
- Smartt S. J., 2009, *ARA&A*, **47**, 63
- Smartt S. J., 2015, *Publ. Astron. Soc. Australia*, **32**, e016
- Smartt S. J., Maund J. R., Hendry M. A., Tout C. A., Gilmore G. F., Mattila S., Benn C. R., 2004, *Science*, **303**, 499
- Smartt S. J., Eldridge J. J., Crockett R. M., Maund J. R., 2009, *MNRAS*, **395**, 1409

- Smartt S. J., et al., 2015, *A&A*, **579**, A40
- Spiro S., et al., 2014, *MNRAS*, **439**, 2873
- Straniero O., Dominguez I., Piersanti L., Giannotti M., Mirizzi A., 2019, *ApJ*, **881**, 158
- Taddia F., et al., 2016, *A&A*, **588**, A5
- Takáts K., et al., 2014, *MNRAS*, **438**, 368
- Takáts K., et al., 2015, *MNRAS*, **450**, 3137
- Terreran G., et al., 2016, *MNRAS*, **462**, 137
- Terreran G., et al., 2017, *Nature Astronomy*, **1**, 713
- Tomasella L., et al., 2013, *MNRAS*, **434**, 1636
- Tomasella L., et al., 2018, *MNRAS*, **475**, 1937
- Tsvetkov D. Y., et al., 2019, *MNRAS*, **487**, 3001
- Tsvetkov D. Y., et al., 2021, *Astronomy Letters*, **47**, 291
- Utrobin V. P., 2004, *Astronomy Letters*, **30**, 293
- Utrobin V. P., Chugai N. N., 2008, *A&A*, **491**, 507
- Utrobin V. P., Chugai N. N., 2009, *A&A*, **506**, 829
- Utrobin V. P., Chugai N. N., 2019, *MNRAS*, **490**, 2042
- Utrobin V. P., et al., 2021, *MNRAS*, **505**, 116
- Valenti S., et al., 2016, *MNRAS*, **459**, 3939
- Van Dyk S. D., 2017, *Philosophical Transactions of the Royal Society of London Series A*, **375**, 20160277
- Van Dyk S. D., Li W., Filippenko A. V., 2003, *PASP*, **115**, 1289
- Van Dyk S. D., et al., 2019, *ApJ*, **875**, 136
- Williams B. F., Peterson S., Murphy J., Gilbert K., Dalcanton J. J., Dolphin A. E., Jennings Z. G., 2014, *ApJ*, **791**, 105
- Williams B. F., Hillis T. J., Murphy J. W., Gilbert K., Dalcanton J. J., Dolphin A. E., 2018, *ApJ*, **860**, 39
- Wolfinger K., Kilborn V. A., Koribalski B. S., Minchin R. F., Boyce P. J., Disney M. J., Lang R. H., Jordan C. A., 2013, *MNRAS*, **428**, 1790
- Woolley S. E., Weaver T. A., 1995, *ApJS*, **101**, 181
- Woolley S. E., Heger A., Weaver T. A., 2002, *Reviews of Modern Physics*, **74**, 1015
- Yamanaka M., Nakaoka T., Kawabata M., Kimura H., Kawabata K. S., 2018, *The Astronomer's Telegram*, **11526**, 1
- Yang S., et al., 2021, *A&A*, **655**, A90
- Yuan F., et al., 2016, *MNRAS*, **461**, 2003
- Yuan W., et al., 2020, *ApJ*, **902**, 26
- Zapartas E., de Mink S. E., Justham S., Smith N., Renzo M., de Koter A., 2021, *A&A*, **645**, A6
- Zgirski B., et al., 2021, *ApJ*, **916**, 19

APPENDIX A: SNe 2015bs and 2018aoq

Here I estimate distances, reddenings, explosion epochs, absolute magnitudes, and ^{56}Ni masses for SNe 2015bs and 2018aoq using the same methodology as in Rodríguez et al. (2021). For this, I use photometric and spectroscopic data presented by O'Neill et al. (2019) and Tsvetkov et al. (2019, 2021) for SN 2018aoq, and by Anderson et al. (2018) for SN 2015bs.

SN 2018aoq was discovered in NGC 4151 ($cz = 997 \text{ km s}^{-1}$, Wolfinger et al. 2013) by the Lick Observatory Supernova Search on 2018 April 01.436 UT (Nazarov et al. 2018). The SN, also visible in pre-explosion images taken on March 31.962 UT (Nazarov et al. 2018), was not detected on March 31.5 UT (Yamanaka et al. 2018). Using the last non-detection and the first detection epoch, along with optical spectroscopy and the SNII_ETOS code¹¹ (Rodríguez et al. 2019), the explosion epoch is estimated to be MJD 58208.74 \pm 0.14. I adopt the SN Ia distance modulus of 30.99 \pm 0.06 mag measured by Yuan et al. (2020), and a Galactic reddening

of 0.023 \pm 0.004 mag (Schlafly & Finkbeiner 2011). I derive a host galaxy reddening of 0.085 \pm 0.066 mag using the colour method (Olivares E. et al. 2010), 0.115 \pm 0.058 mag using the colour-colour method (Rodríguez et al. 2014, 2019) implemented in the C3M code,¹² and 0.0 \pm 0.1 mag using the spectrum-fitting technique (e.g. Olivares E. et al. 2010; Rodríguez et al. 2021). I adopt the weighted average of these three values (0.086 \pm 0.040 mag) as the host galaxy reddening for SN 2018aoq. I compute $M_R^{\text{max}} = -16.029$ and $M_V^{50d} = -15.613 \pm 0.136$. Using the *I*-band photometry in the radioactive tail and the SNII_nicel code¹³ (Rodríguez et al. 2021), I measure a $\log(M_{\text{Ni}}/M_{\odot})$ value of -2.022 ± 0.058 dex. This value, equivalent to $M_{\text{Ni}} = 0.0096 \pm 0.0013 M_{\odot}$, compares to the ^{56}Ni mass of 0.01 M_{\odot} adopted by Tsvetkov et al. (2021) for their radiation-hydrodynamical simulations.

SN 2015bs was discovered by the Catalina Real-Time Transient Survey on 2014 September 25 UT, being not detected ten days before the discovery (Anderson et al. 2018). The Galactic reddening toward the SN is of 0.044 \pm 0.007 mag (Schlafly & Finkbeiner 2011), while the heliocentric redshift is of 0.027 (Anderson et al. 2018). Using the Hubble law with a local Hubble constant of 74.03 \pm 1.42 $\text{km s}^{-1} \text{ Mpc}^{-1}$ (Riess et al. 2019) and a velocity dispersion of 382 km s^{-1} to account for the effect of peculiar velocities over distances, I compute a distance modulus of 35.10 \pm 0.11 mag. I estimate the explosion epoch to be MJD 56921.53 \pm 2.57 using the SNII_ETOS code. The host galaxy reddening computed with the spectrum-fitting technique is of 0.0 \pm 0.1 mag. I calculate $M_R^{\text{max}} = -17.47$ and $M_V^{50d} = -16.988 \pm 0.325$. To estimate M_{Ni} , I first convert the Pan-STARRS1 *w*-band photometry to *R*-band magnitudes. For this, I use the methodology described in Rodríguez et al. (2021), finding a transformation given by $w - R = 0.41 \pm 0.04$ mag for the radioactive tail. Using the *R*-band magnitudes in the radioactive tail and the SNII_nicel code, I compute $\log(M_{\text{Ni}}/M_{\odot}) = -1.156 \pm 0.119$ dex, equivalent to $M_{\text{Ni}} = 0.072 \pm 0.020 M_{\odot}$. This estimate is statistically consistent with the ^{56}Ni mass of 0.049 \pm 0.008 M_{\odot} reported in Anderson et al. (2018).

This paper has been typeset from a $\text{\TeX}/\text{\LaTeX}$ file prepared by the author.

¹¹ https://github.com/olrodrig/SNII_ETOS

¹² <https://github.com/olrodrig/C3M>

¹³ https://github.com/olrodrig/SNII_nicel